High resolution low-energy diffraction on graphite and galliumarsenide

van Beckhoven, M.W.C.

Award date:
1990

High Resolution
Low-Energy Electron Diffraction
on
Graphite and Galliumarsenide

M.W.C. van Beckhoven july 1989

Master thesis
Eindhoven University of Technology
Department of Physics
Solid State Division
Surface Physics Group

Coached by H.H. Brongersma
A.G. Roosenbrand

Abstract

In this work experiments with a high-resolution spot profile analysis (SPA) LEED system have been performed on the surface of highly oriented pyrolytic graphite and the (001) surface of gallium-arsenide. In diffraction experiments one operates in reciprocal space. Therefore, the angular intensity distribution within a single spot reveals diffraction effects originating from topological features at the sample surface. The high-resolution SPA-LEED system equipped with an accurate and stable sample manipulator is very well suited for the determination of the angular intensity distribution within a large scale of reflections.

Experiments on HOPG have revealed that the crystallites in the surface have an angular spread of $0.3° - 0.5°$ out of the surface plane of the sample, intrinsic to HOPG or induced by the cleaving procedure. The orientations of the crystallites distributes the first and higher order reflections over rings with centre at the origin of reciprocal space. These rings contain maxima originating from preferential orientations of the crystallites. For the specular reflection the maximum intensity has been measured as function of energy. The positions of the peaks closely resemble measurements in literature. The discrepancy at lower energies is due to the different measuring method. Comparing our findings on HOPG with STM measurements, we conclude that the results of SPA-LEED and STM are complementary.

The GaAs(001) surface has been studied with SPA-LEED for reconstruction and step height. The observed diffraction spots for energies above 100 eV at room temperature originate form the GaAs(001)-(1×1) structure. For energies below 100 eV no diffraction spots have been observed. Furthermore, the profile scans of the direct reflection show a considerable background and reveal no clear sharp reflection. All these observations lead to the conclusion that in our experiment the outermost layer has no long range order at room temperature. This might be due to the contamination of the surface by carbon containing compounds. Profile scans of the direct reflection clearly reveal the shape of a Gaussian at in-phase conditions and the broader shape of a Lorentzian at out-of-phase conditions. Oscillations are measured in the full width at half maximum of the (00) and (11) reflection. These oscillations have a small amplitude and a period consistent with even-numbered atomic step heights. From the oscillations and the fact that the surface consists merely of As atoms, it is concluded that a limited number of even-numbered atomic steps exists on the GaAs(001) surface.

Samenvatting

Tijdens dit afstudeerwerk zijn experimenten verricht met behulp van een hoge resolutie SPA-LEED apparaat (Spot Profile Analysis of Low-Energy Electron Diffraction) aan grafiet en aan gallium-arsenide. In diffractie experimenten wordt gewerkt in de reciproke ruimte. Hierdoor bevat de intensiteitsverdeling binnen een diffractie spot informatie over topologische verschijnselen op het preparaat oppervlak. Het SPA-LEED systeem is toegerust met een zeer nauwkeurige preparaat manipulator, waardoor de intensiteitsverdeling van een groot aantal reflecties opgemeten kan worden.

Uit experimenten aan highly oriented pyrolytic graphite (HOPG) is gebleken dat de afzonderlijke krystallieten in het oppervlak onder een hoek ($0.3° - 0.5°$) geöriënteerd zijn ten opzichte van het grofstoffelijke oppervlak. Deze hoek spreiding is ofwel intrinsiek aan HOPG of een gevolg van het klievingsproces. Door de willekeurige oriëntatie van de krystallieten in het oppervlak zijn de eerste en hogere orde reflecties uitgesmeerd over ringen. In deze ringen komen maxima voor, die duiden op voorkeursrichtingen van de oriëntaties. De intensiteit van de directe reflectie is opgemeten als functie van de energie. De posities van de maxima in deze curve corresponderen met metingen uit de literatuur. De grotere afwijking in maxima posities bij lagere energiën is veroorzaakt door het verschil in meetmethode. Vergelijking van de meetresultaten verkregen met Scanning Tunneling Microscopy (STM) en SPA-LEED leidt tot de conclusie dat de technieken elkaar aanvullende informatie verschaffen met betrekking tot het HOPG oppervlak.

Het GaAs(001) oppervlak is onderzocht met SPA-LEED op reconstructie van het oppervlak en op het voorkomen van stappen. De waargenomen reflecties voor energiën boven 100 eV zijn afkomstig van de GaAs(001)-(1×1) structuur. Voor energiën lager dan 100 eV zijn geen diffractie spots gedetecteerd. De spotprofielen van de directe reflectie opgenomen boven 100 eV vertonen een hoge achtergrond, terwijl geen duidelijke scherpe reflectie aanwezig is. Uit al deze waarnemingen mag geconcludeerd worden dat het oppervlak geen long range order bevat bij kamertemperatuur. Dit is mogelijk een gevolg van vervuiling van het oppervlak met koolwaterstoffen. De spotprofielen kunnen gefit worden met een Gauss kromme voor in-fase verstrooiing condities van de terrassen. De uit-fase verstrooiing conditie voor de terrassen geeft duidelijk aanleiding tot een verbreding van het profiel. In dit geval zal het spotprofiel met een Lorentz krommes gefit moeten worden. De oscillaties in de spotbreedte als functie van energie hebben een kleine amplitude en een periode overeenkomstig met dubbel atomaire stappen op het oppervlak. Uit LEIS metingen (Low-Energy Ion Scattering) is gebleken dat het GaAs(001) oppervlak voornamelijk uit As atomen bestaat. Uit de LEIS metingen en de spotbreedte oscillaties mag geconcludeerd worden dat het oppervlak een beperkt aantal stappen bevat van voornamelijk een dubbel atomaire staphoogte.

Contents

Chapter 1

Introduction

The surface of a solid at an interface may have properties that are considerably different from the bulk. Generally spoken these differences can be caused by relaxation, reconstruction or segregation. In surface physics the main emphasis lays on the study of the solid-vacuum interface.

A large variety of surface sensitive techniques exists in order to analyse the surface. Most of them are based on the observation of the interaction of particles (including photons) with the surface. A few of those techniques will be shortly discussed.

In X-ray Photoelectron Spectroscopy (XPS) an electron is emitted by the absorption of a photon. From the kinetic energy of the electron, the electron binding energy inside the surface atom can be derived. This binding energy is specific for each element, so one can obtain the surface composition. Using Auger Electron Spectroscopy (AES) a core level electron can be removed with either photons or electrons. The vacancy in the core level will be filled with an outer shell electron, in combination with the simultaneous excitation of an Auger electron or a photon. The Auger electron energy is characteristic for a specific atom. Both techniques (XPS and AES) are surface sensitive because of the short mean free path of the electron in the concerned energy region. Low-Energy Ion Scattering (LEIS), also called Ion Scattering Spectroscopy (ISS), is a surface sensitive technique in which a surface is bombarded with ions of low energy. From the energy of the back-scattered ions the mass of the surface atoms can be calculated. The principle of Scanning Tunneling Microscopy (STM) is straightforward. It consists essentially of scanning a metal tip over the surface at a constant tunnel current. The displacements of the metal tip given by the voltages applied to piezo-drives then yield a topografic picture of the surface.

Experiments with Low-Energy Electron Diffraction (LEED) provide the surface periodicity of crystals. In LEED experiments a monochromatic electron beam ($30 \leq E \leq 500$ eV) is diffacted at the crystal surface. Due to the limited penetration depth of electrons for this energy region, LEED is highly surface sensitive. In diffraction experiments one operates in reciprocal space. Therefore the angular intensity distribution within a single spot reveals diffraction effects originating from topological features at the sample surface. The high-resolution Spot Profile Analysing (SPA) LEED system is very well suited to measure the intensity distribution in a spot. If high energy is used, gracing incidence is needed, to reduce the (projected) penetration depth for surfac sensitivity. This method is known as Reflection High-Energy Electron Diffraction. RHEED is sensitive to topological features in the surface such as epitaxial growth. It is often used to control crystal growth with Molecular

Beam Epitaxy (MBE).

The last three techniques will be discussed in chapter 2. In chapter 3 some reflections are given on the complementarity of STM and (SPA)LEED on the basis of experiments on graphite. Within the framework of the micro-electronics project the (001) surface of the semiconductor galliumarsenide was investigated. The results will be reported in chapter 4. Chapter 5 contains a brief summary of the most important conclusions and recommandations for further investigations.

Chapter 2

SPA-LEED

2.1 Introduction

The experimental observation of low-energy electron diffraction was first made by Davisson and Germer in 1927 [DAV27]. LEED provides information about the surface symmetry of solid crystals. In a LEED experiment a monochromatic electron beam is diffracted at the crystal surface (fig. 2.1). The electron beam interacts strongly with matter and thus cannot

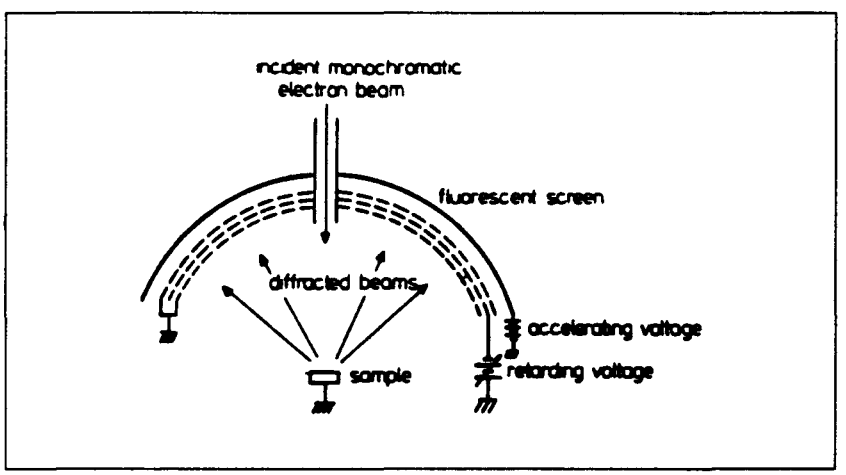

Figure 2.1: *Scheme of LEED-apparatus*

penetrate very deeply (fig. 2.2). The elastically back-scattered electrons are diffracted in certain directions, caused by the wave character of electrons. The de Broglie wavelength of an electron with velocity v is given by:

$$\lambda = \frac{h}{mv} \tag{2.1}$$

where h is Planck's constant.
If E is the energy of an electron eq. 2.1 can be written as:

$$\lambda = \sqrt{\frac{1.504}{E(\text{eV})}} \quad (\text{nm}) \tag{2.2}$$

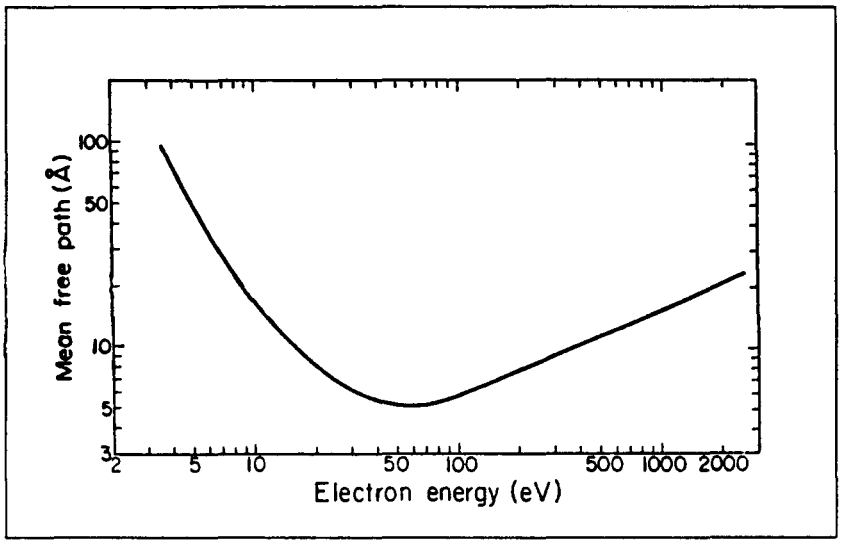

Figure 2.2: *Variation in mean escape depth with increasing electron energy*

For energies between about 30 and 500 eV, the electron wavelengths are comparable to the typical lattice spacing of crystals. These two factors - a limited penetration depth and a suitable wavelength - are the basic reasons why LEED is considered to be a suitable probe for surface geometrical structures.

The LEED pattern can always be described by the kinematic theory (section 2.2). This is because the scattered beam directions are determined solely by the relative phase of reflected waves emanating from scattering atoms equivalent under the periodic translation of the surface. This relative phase depends on the unit cell dimensions, but not on the scattering mechanism. The scattering mechanism, whether kinematic or dynamical, influences only the absolute phase and the intensity of the reflected waves. Therefore, LEED spots always have positions that can de determined kinematically.

Deviations of an ideal surface are reflected in the angular intensity distribution of the diffracted electrons. Spot Profile Analysing LEED provides the high resolution in order to measure the intensity distribution in a spot.

2.2 Kinematic description of diffraction

Kinematic diffraction is the situation in which each wave packet representing one electron incident on a surface is diffracted elastically only once by that surface.

2.2.1 Diffraction and the reciprocal lattice

Diffraction results from the interaction between the periodic oscillations of a wavefield and a periodic array of scattering centres. The periodicity of the waves and scatterers provide a number of different possible conditions at which strong in-phase scattering occurs. In fig. 2.3 a plane wave is incident on an one-dimensional lattice at an angle θ_0. Taking only elastical

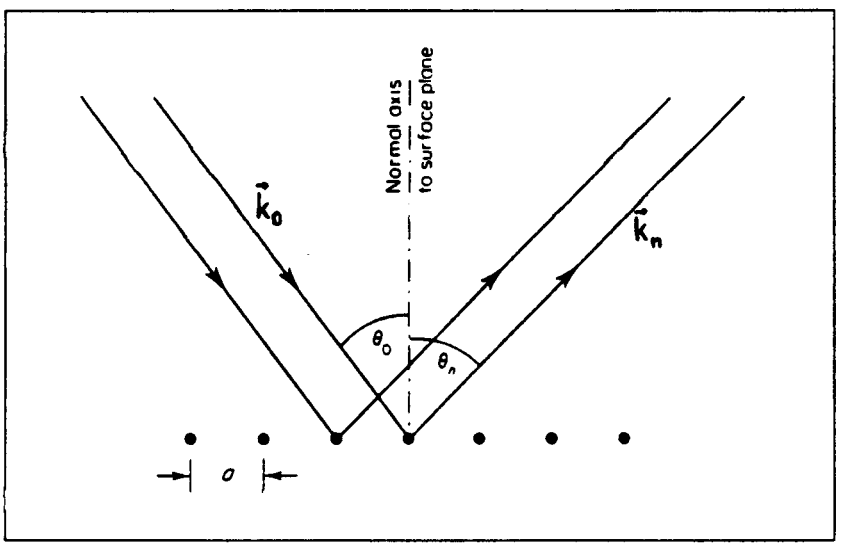

Figure 2.3: *Diffraction from a one-dimensional array of scatterers*

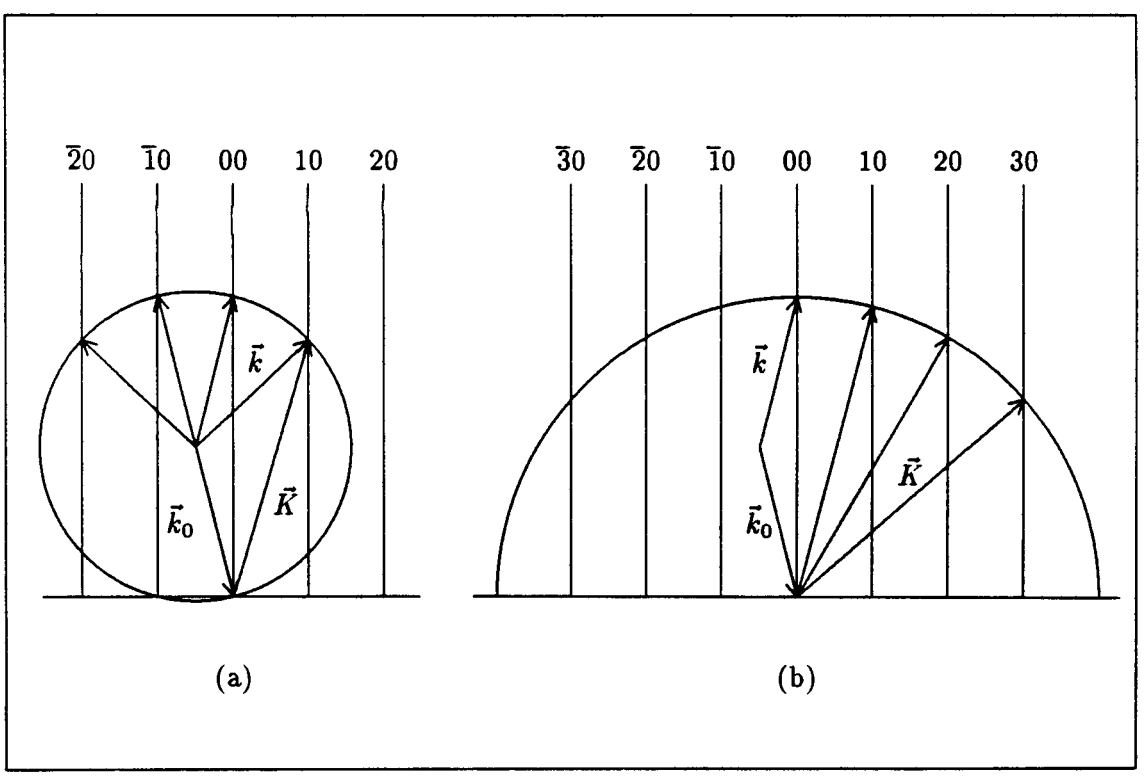

Figure 2.4: *The Ewald construction in one-dimension using conventional LEED (a) or SPA-LEED (b)*

diffraction in consideration, the following equation holds:

$$|\vec{k}_0| = |\vec{k}| = \sqrt{\frac{2m}{\hbar^2}E} \tag{2.3}$$

where $\vec{k}_0$ and $\vec{k}$ are resp. the wave vectors of the incident and the emergent beams.
The in-phase condition is met for all situations which satisfy the condition:

$$\vec{a} \cdot (\vec{k} - \vec{k}_0) = \vec{a} \cdot \vec{K} = 2\pi h \tag{2.4}$$

where $\vec{a}$ is the lattice constant and h is an integer.
Eq. 2.4 is referred to as a Laue condition. The Laue condition implies that constructive interference occurs at planes (h) perpendicular to the reciprocal lattice vector $\vec{a}^*$ intersecting the points $h|\vec{a}^*|$. When a two-dimensional system is taken in consideration, two Laue conditions are found, each representing a row of planes. Constructive interference then takes place at the intersections of the planes, which form the reciprocal lattice rods (hk). With a three-dimensional system the lattice rods turn into lattice points (hkl). The possible scatter directions can be found with help of the Ewald construction [ASH76]. The condition for elastical scattering and the relevant Laue condition(s) are constructed graphically in reciprocal space. The Ewald construction for LEED, SPA-LEED and RHEED will be discussed.

The reciprocal lattice rods (hk) are constructed perpendicular to the surface. The incident beam is represented by the wave vector $\vec{k}_0$, which touches the surface at the origin of the reciprocal lattice. In case of LEED (fig. 2.4.a) the Ewald sphere is constructed with its centre at the initial point of $\vec{k}_0$ and radius $|\vec{k}_0|$. The possible emergent wave vectors $\vec{k}_n$ have the same initial point as $\vec{k}_0$ and end on an intersection of the Ewald sphere with a reciprocal lattice rod.

Using SPA-LEED (fig. 2.4.b) the angle between $\vec{k}_0$ and $\vec{k}$ is fixed at 7.5 degrees (see also section 2.3). As a result the length of $\vec{K}$ is a constant and the Ewald sphere turns into the modified Ewald sphere, i.e. a half sphere with centre at the origin of the reciprocal lattice and radius $|\vec{K}|$.

If high energy is used, gracing incidence is needed, to reduce the (projected) penetration depth for surface sensitivity. This method is known as Reflection High-Energy Electron Diffraction (RHEED). Because of the high velocity of the RHEED-electrons eq. 2.2 should be modified:

$$\lambda = \sqrt{\frac{1.504}{E + 9.78 \cdot 10^{-7} E^2}} \quad \text{(nm)} \tag{2.5}$$

With high energy the radius of the Ewald sphere becomes very large. If the crystal surface contains topological defects, the reciprocal lattice rods will have a finite width. In that case the intersections of the Ewald sphere and the rods are streaks in stead of spots (fig. 2.5).

2.2.2 Kinematic description of diffraction

Low energy electrons are scattered very strongly by the atoms or ions cores in a crystal surface. To account for all features of diffraction, including multiple scattering, the so called dynamical theory has to be applied. However, numerous cases can satisfactorily be described by the single scattering kinematical theory. This kinematical theory has been thoroughly described in [WEB73, HEN77, CLA84, ERT85, HOV86, ROO87]. In this subsection a summary of the most important aspects of the kinematical theory will be given.

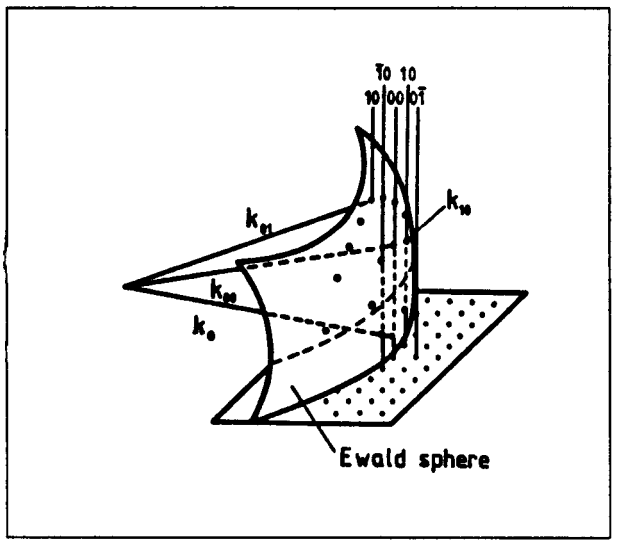

Figure 2.5: *Ewald construction using RHEED*

A monoenergetic electron beam is represented by a plane wave:

$$\Psi = \Psi_0 \exp[i\vec{k}_0 \cdot \vec{r}] \tag{2.6}$$

where Ψ_0 is the amplitude of the incident wave, $\vec{k}_0$ is the wave vector of the incident beam and $\vec{r}$ is a space vector. If the electron beam is diffracted by an array of scattering centres, the contribution of one scattering centre at position $\vec{r}_i$, at a large distance R from the sample is:

$$\Psi_i(\vec{R}) = \Psi_0 \frac{\exp[i\vec{k} \cdot \vec{R}]}{|\vec{R} - \vec{r}_i|} f_i(\vec{k}_0, \vec{k}) \exp[i\vec{K} \cdot \vec{r}_i] \tag{2.7}$$

where $f_i(\vec{k}_0, \vec{k})$ is the scattering factor, which for a given kind of atom depends on the incident wavevector $\vec{k}_0$ and emergent wavevector $\vec{k}$ and therefore on the wavelength and the direction of the incident and emergent waves. Summation of all scattering contributions and the approximation $|\vec{R} - \vec{r}_i| \sim |\vec{R}|$ yields for the total diffracted beam:

$$\Psi(\vec{R}) = \Psi_0 \frac{\exp[i\vec{k} \cdot \vec{R}]}{|\vec{R}|} \sum_i f_i(\vec{k}_0, \vec{k}) \exp[i\vec{K} \cdot \vec{r}_i] \tag{2.8}$$

From eq. 2.8 the observed intensity can be calculated by:

$$I(\vec{K}) = \Psi(\vec{R})\Psi^*(\vec{R}) = I_0 \sum_{i,j} f_i(\vec{k}_0, \vec{k}) f_j^*(\vec{k}_0, \vec{k}) \exp[i\vec{K} \cdot (\vec{r}_i - \vec{r}_j)] \tag{2.9}$$

which reduces for identical scatterers to:

$$I(\vec{K}) = N I_0 |f(\vec{k}_0, \vec{k})|^2 + I_0 |f(\vec{k}_0, \vec{k})|^2 \sum_{i \neq j} \exp[i\vec{K} \cdot (\vec{r}_i - \vec{r}_j)] \tag{2.10}$$

The first term is just the scattering from N independently scattering atoms. All the information about the interference is contained in the second term. In case of a crystal with

$M_1 \cdot M_2 \cdot M_3$ lattice points located at $\vec{r}_i = m_1\vec{a} + m_2\vec{b} + m_3\vec{c}$ $(1 \leq m_i \leq M_i)$ and with atoms located within each unit cell at positions $\vec{u}_i$ eq. 2.8 can be written as:

$$\Psi(\vec{K}) \sim \sum_{n=0}^{N-1} f_n(\vec{k}_0, \vec{k}) \exp[i\vec{K} \cdot \vec{u}_n] \sum_i \exp[i\vec{K} \cdot \vec{r}_i]$$

$$\Psi(\vec{K}) \sim F(\vec{k}_0, \vec{k}) \cdot G(\vec{K}) \tag{2.11}$$

$$F(\vec{k}_0, \vec{k}) = \sum_{n=0}^{N-1} f_n(\vec{k}_0, \vec{k}) \exp[i\vec{K} \cdot \vec{u}_n] \tag{2.12}$$

$$G(\vec{K}) = \sum_{m_1=1}^{M_1} \exp[i\vec{K} \cdot m_1\vec{a}] \sum_{m_2=1}^{M_2} \exp[i\vec{K} \cdot m_2\vec{b}] \sum_{m_3=1}^{M_3} \exp[i\vec{K} \cdot m_3\vec{c}] \tag{2.13}$$

where $F(\vec{k}_0, \vec{k})$ is the crystal structure factor and $G(\vec{K})$ is the crystal lattice factor.

The observed intensity can now be written as:

$$I(\vec{K}) = |F(\vec{k}_0, \vec{k})|^2 \cdot |G(\vec{K})|^2 \tag{2.14}$$

where $|G(\vec{K})|^2$ is the interference function. This function is often denoted in literature as $G(\vec{K})$ or $\mathcal{I}(\vec{K})$. The interference function reproduces the arrangement of scatterers. The structure factor $F(\vec{k}_0, \vec{k})$ contains all information on the scattering properties of a single atom, including multiple scattering.

A crystal may be described by units consisting of one or several surface atoms and all underlying atoms (columns) [HEN85]. For a periodic surface all columns are identical. If a surface is disordered, not all columns are exactly the same. For example the columns 5, 6 and 7 in fig 2.6 are not identical. The structure factor $F(\vec{k}_0, \vec{k})$ is giving the intensity

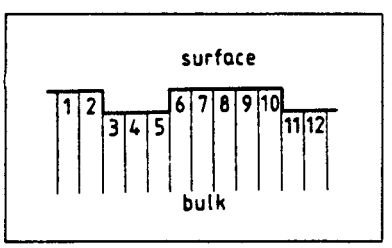

Figure 2.6: *A cross section of a surface showing columns*

coming from a single unit including all multiple scattering contributions within the column or via neighbouring columns. The interference function $|G(\vec{K})|^2$ describes the positions of the spots. If all columns are identical and the structure factor F varies only slowly with energy, the profile of a spot is given by the interference function. In the kinematic approximation the differences of the units according to their individual neighbourhoods are neglected. This means that in fig 2.6 the columns 5, 6 and 7 are considered to be identical with respect to the structure factor. Within this approximation the diffraction is therefore completely determined by the interference function $|G(\vec{K})|^2$ [HEN77]. The validity of the kinematic calculation may be checked by measuring the spot profile for different spots and energies. If a strict periodicity with the vectors of the reciprocal space is observed, the kinematic approximation with identical structure factors F is justified. So far no experimental results are reported which require dynamic calculations with respect to disorder.

In the LEED experiment only the intensity is available. In order to obtain the interference function, the structure factor is eliminated by comparing the intensity with its integral over a Brillouin zone (BZ) [HOR88, ALT88]:

$$\begin{aligned}\frac{I(\vec{K})}{\int\limits_{BZ} I(\vec{K})dK_{\|}} &= \frac{|F(\vec{k}_0,\vec{k})|^2|G(\vec{K})|^2}{\int\limits_{BZ}|F(\vec{k}_0,\vec{k})|^2|G(\vec{K})|^2dK_{\|}} \\ &\sim \frac{|F(\vec{k}_0,\vec{k})|^2|G(\vec{K})|^2}{\langle|F(\vec{k}_0,\vec{k})|^2\rangle\int\limits_{BZ}|G(\vec{K})|^2dK_{\|}} \\ &= \frac{|F(\vec{k}_0,\vec{k})|^2}{\langle|F(\vec{k}_0,\vec{k})|^2\rangle}|G(\vec{K})|^2 \sim |G(\vec{K})|^2 \end{aligned} \tag{2.15}$$

with $\langle|F(\vec{k}_0,\vec{k})|^2\rangle$ is the weighted average of the structure factor and the use of the following equation:

$$\int\limits_{BZ}|G(\vec{K})|^2dK_{\|} = constant = 1 \tag{2.16}$$

This value is the whole intensity scattered from one unit cell into one Brillouin zone and it is independent of the spatial arrangement of unit cells. From the interference function, available from the experiment in this way, both the lateral distribution (island size, terrace length) as well as the vertical distribution (roughness, layer distribution) can be determined.

In the previous subsection (2.2.1) conditions for constructive interference have been deduced. These so-called Laue conditions can be derived from the interference function $|G(\vec{K})|^2$. With the help of 2.13 and the following equation:

$$\sum_{n=0}^{N-1} x^n = \frac{1-x^N}{1-x} \tag{2.17}$$

the interference function can be written as:

$$|G(\vec{K})|^2 = \frac{\sin^2\frac{1}{2}M_1\vec{K}\cdot\vec{a}}{\sin^2\frac{1}{2}\vec{K}\cdot\vec{a}}\frac{\sin^2\frac{1}{2}M_2\vec{K}\cdot\vec{b}}{\sin^2\frac{1}{2}\vec{K}\cdot\vec{b}}\frac{\sin^2\frac{1}{2}M_3\vec{K}\cdot\vec{c}}{\sin^2\frac{1}{2}\vec{K}\cdot\vec{c}} \tag{2.18}$$

The interference function has maxima when $\vec{K}$ satisfies the three Laue conditions:

$$\vec{K}\cdot\vec{a} = 2\pi h \tag{2.19}$$

$$\vec{K}\cdot\vec{b} = 2\pi k \tag{2.20}$$

$$\vec{K}\cdot\vec{c} = 2\pi l \tag{2.21}$$

Using the reciprocal lattice vector $\vec{g}_{hkl} = h\vec{a}^* + k\vec{b}^* + l\vec{c}^*$ the Laue conditions turn into:

$$\vec{K} = \vec{k} - \vec{k}_0 = \vec{g}_{hkl} \tag{2.22}$$

The kinematic approximation of LEED only takes into account scattering of electrons at the crystal surface region, so in that case the third Laue condition is left out and only components parallel to the crystal surface remain:

$$\vec{K}_{\|} = \vec{k}_{\|} - \vec{k}_{0\|} = \vec{g}_{hk} = h\vec{a}^* + k\vec{b}^* \tag{2.23}$$

With the condition for elastical scattering (eq. 2.3) the expression for the wave vector of the emergent beam is:

$$\vec{k}^{\pm} = \begin{pmatrix} k_{0x} + g_x \\ k_{0y} + g_y \\ \pm\sqrt{\frac{2m}{\hbar^2} E - |k_{0\|} + g_{hk}|^2} \end{pmatrix} \tag{2.24}$$

However, a beam of low energy electrons incident on a crystal surface is strongly attenuated, but still has a certain penetration depth. A modification of the kinematic description of diffraction can be made in order to include this penetration depth. In the so-called Darwin approximation the attenuation is described by the factor α, which is defined as the ratio of the amplitudes contributed to the scattered beam by atoms in successively deeper layers n [WEB73]:

$$\alpha = \frac{A_{n+1}}{A_n} \tag{2.25}$$

The factor α will in general depend on the energy of the electrons. With eq. 2.25 the lattice factor (eq. 2.13) becomes:

$$\begin{aligned} G(\vec{K}) &= \sum_{m_1=1}^{M_1} \exp[i\vec{K}\cdot m_1\vec{a}] \sum_{m_2=1}^{M_2} \exp[i\vec{K}\cdot m_2\vec{b}] \sum_{m_3=1}^{M_3} \alpha^{m_3}\exp[i\vec{K}\cdot m_3\vec{c}] \\ G(\vec{K}) &= \sum_{m_1=1}^{M_1} \exp[i\vec{K}\cdot m_1\vec{a}] \sum_{m_2=1}^{M_2} \exp[i\vec{K}\cdot m_2\vec{b}] \frac{1}{1-\alpha\exp[i\vec{K}\cdot\vec{c}]} \end{aligned} \tag{2.26}$$

which gives for the interference function $|G(\vec{K})|^2$:

$$|G(\vec{K})|^2 = \frac{\sin^2\frac{1}{2}M_1\vec{K}\cdot\vec{a}}{\sin^2\frac{1}{2}\vec{K}\cdot\vec{a}} \frac{\sin^2\frac{1}{2}M_2\vec{K}\cdot\vec{b}}{\sin^2\frac{1}{2}\vec{K}\cdot\vec{b}} \frac{1}{1+\alpha^2-2\alpha\cos\vec{K}\cdot\vec{c}} \tag{2.27}$$

The Laue condition (eq. 2.23) still holds, which means that the diffracted intensity is confined

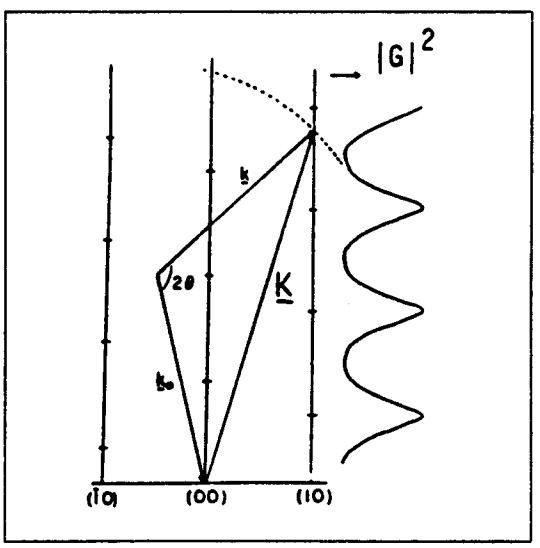

Figure 2.7: *Modulation of the interference function*

to directions along the reciprocal lattice rods (hk). The effect of the shallow penetration of the electron wave packets is a modulation of the interference function along the reciprocal lattice rods, with broad maxima at positions where the third Laue condition (eq. 2.21) is satisfied (fig. 2.7), shifted by the inner potential (see section 2.2.3).

2.2.3 Inner potential

When electrons enter a crystal from the vacuum, they are influenced by a periodic potential in the crystal half space:

$$V_0 = V_{0r} + iV_{0i} \tag{2.28}$$

where V_{0r} is the inner potential and $V_{0i} > 0$ is the imaginary part of the potential used to present all inelastic effects. The inner potential is a spatial average of the actual potential felt by the incident and emergent electrons.
As a result the wave vector of the electrons penetrating the surface changes from the value:

$$\vec{k}_0 = 2\pi\sqrt{\frac{E}{1.504}} \tag{2.29}$$

in the vacuum, to a higher value:

$$\vec{k}_{in} = 2\pi\sqrt{\frac{E + |V_{0r}|}{1.504}} \tag{2.30}$$

in the crystal.
Since there is no force parallel to the crystal surface, the parallel component of the wave vector is conserved and the electron beam is refracted into the crystal as if there were a refractive index:

$$n = \frac{\vec{k}_{in}}{\vec{k}_0} = \left(1 + \frac{|V_{0r}|}{E}\right)^{\frac{1}{2}} \tag{2.31}$$

As a consequence of the higher value of the wave vector in the crystal, the third Laue

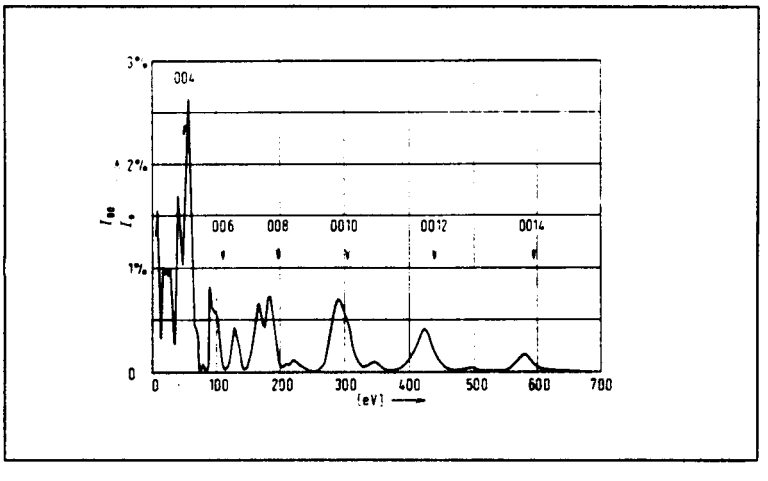

Figure 2.8: *Intensity of (00)-spot of Ni(100) versus electron energy*

condition is satisfied by lower energies of the primary beam than the predicted energies E_{hk}.

In a I-V-curve the maximum intensities will therefore appear at energies $E_{hk} - |V_{0r}|$. The inner potential varies slightly with electron energy. It is found to be greater at low incident energies than at high incident energies. The value of V_{0r} is in the range -30 eV $\leq V_{0r} \leq$ -10 eV, depending on the kind of sample. In Fig. 2.8 an example is given.

2.2.4 Diffraction from defect surfaces

In this subsection a review is presented of surface defects and their influence on the LEED profiles. In subsection 2.2.5 the most important surface defect: a step, will be discussed in detail.

Up till now only ideal surfaces have been considered. An ideal surface is strictly periodic in two dimensions. Deviations from the ideal surface can be classified by dimension. Point defects as vacancies are zero-dimensional defects, which may occur randomly or correlated. One-dimensional defects are the border lines of limited two-dimensional entities (like terraces or superstructure domains) and two-dimensional defects have periodicities different to that of the ideal surface in absolute value (superstructure) or direction (facets). Three dimensional defects are defects of the bulk and therefore not directly surface defects. Examples of bulk defects are mosaic structures and material strain. All defects have their own effect on the diffracted spot profile, which can be obtained by using SPA-LEED. (fig. 2.9). Besides the

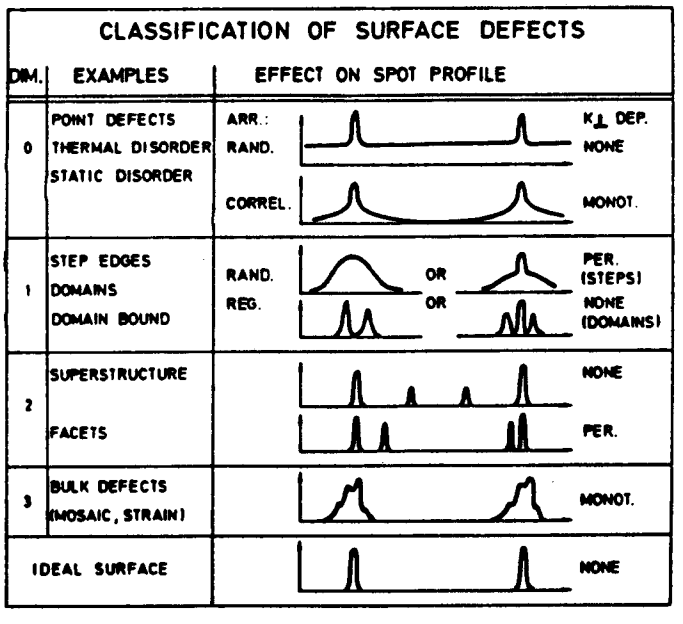

Figure 2.9: *Defect surfaces and their spot profiles. The arrangement (ARR) of the defects is random (RAN), correlated (COR) or regular (REG). The energy dependence on $K_\perp$ can be periodically (PER) or monotonously (MONOT).*

surface defects, other deviations from periodicity occur, being distinguished in chemical compositions (e.g. periodic adlayers), incomplete surface layers and deviations from regular bulk sites (e.g. thermal disorder).

It is clear that the distribution of the atoms in the top layer can be obtained from the spot profiles. In fig 2.10 a two-layer model is given in which the distribution of the atoms in the top layer differ from the periodicity in the second layer. This model can be seen as

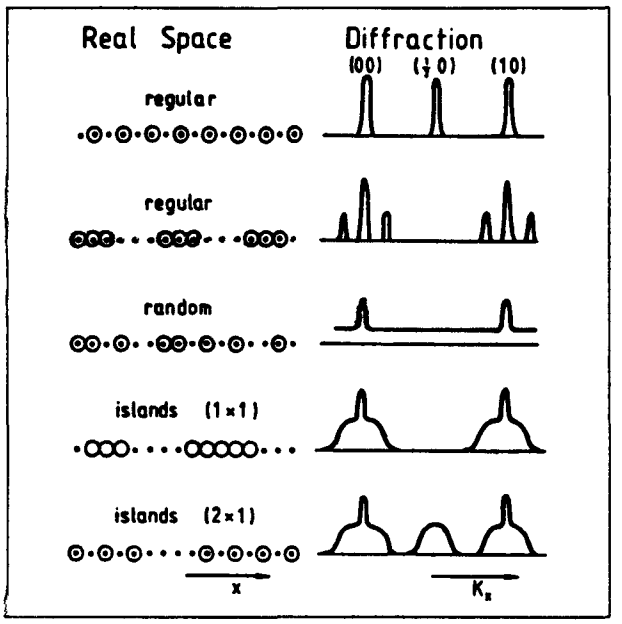

Figure 2.10: *Adlayer distributions and the corresponding spot profiles*

an array of terraces with two levels. In the first case the adlayer (superstructure) has a periodicity twice as large as the second layer, which results in reciprocal lattice rods with separations twice as small. Therefore fractional spots occur (for example $(\frac{1}{2}\ 0)$). When regular terraces are formed, the main spots will show splitting. This effect will be discussed in detail in subsection 2.2.5. Randomly distributed adlayer atoms give rise to a certain background. For terraces of irregular width (islands (1×1)) the spot profile can be divided into two contributions: a sharp reflection and a diffuse intensity profile [MOR87] (see also subsection 2.2.5). The sharp reflection is due to the long range order of the lattice. The diffuse intensity arises from the fluctuation of the scattering amplitudes along the surface. In the last example (islands (2×1)), terraces are formed with periodicity twice as large as the second layer. Therefore in reciprocal space the periodicity is twice as small and diffuse intensity shoulders will arise at half-order positions.

2.2.5 Diffraction from stepped surfaces

Steps at surfaces are very common. High indexed planes often exist of low indexed terraces separated by steps. Since LEED is only sensitive to a few atomic layers, interference occurs between neighbouring terraces due to horizontal and vertical shifts. Those shifts may cause constructive or destructive interference, depending on the energy of the incident beam and angle between incident and emergent waves. In case of constructive interference the spot shape is not changed compared to the ideal flat crystal. At conditions of destructive interference a splitting or broadening of the spot occurs. In fig. 2.11 a one-dimensional model of a stepped surface is given. A regular step array is given by three conditions; constant terrace width, constant step height and constant step orientation. In fig. 2.11 the step is given by the vector $\vec{g}$, the vector $N\vec{a} + \vec{g}$ is the translation vector of the terraces and $\vec{a}$ is the translation vector within a terrace. Given that the surface consists of $n + 1$ terraces the interference function

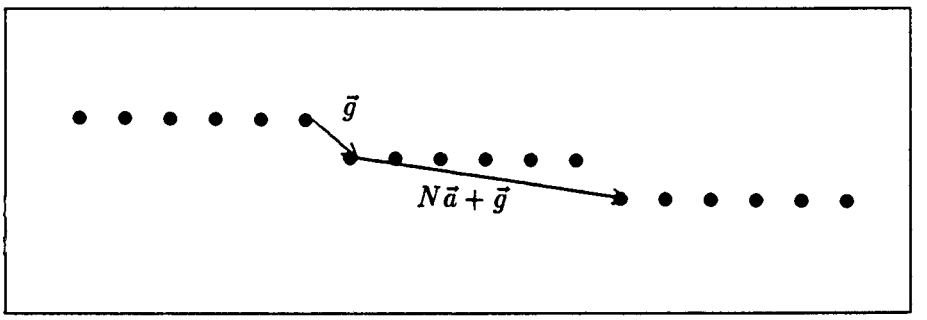

Figure 2.11: *One-dimensional model of a stepped surface*

yields:

$$|G(\vec{K})|^2 = \frac{\sin^2 \frac{N}{2}\vec{K}\cdot\vec{a}}{\sin^2 \frac{1}{2}\vec{K}\cdot\vec{a}} \frac{\sin^2 \frac{n}{2}\vec{K}\cdot(N\vec{a}+\vec{g})}{\sin^2 \frac{1}{2}\vec{K}\cdot(N\vec{a}+\vec{g})} \tag{2.32}$$

The first term at the right hand side represents the square of the structure factor of a single terrace. The second term is the interference function in case of a lattice with lattice constant $N\vec{a}+\vec{g}$. With help of eq. 2.32 the diffraction pattern for the surface is constructed (fig. 2.12). The upper part in the figure shows the diffraction from a single terrace. This intensity

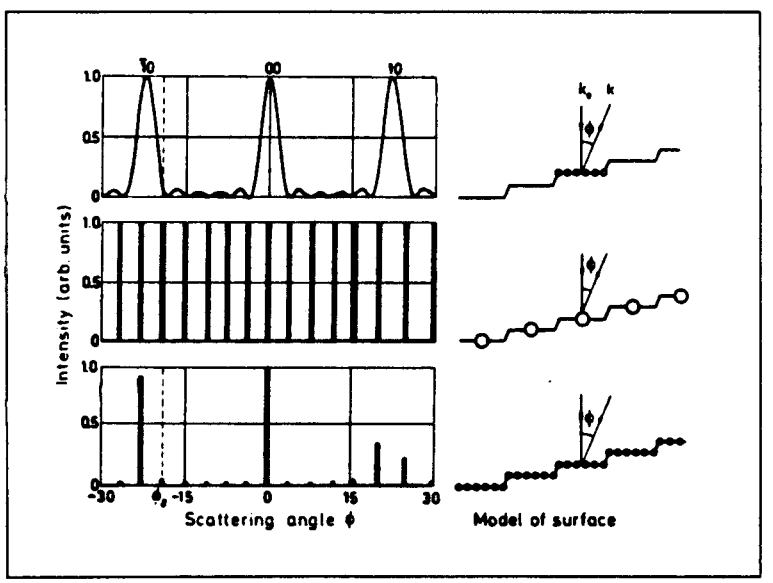

Figure 2.12: *Demonstration of spot splitting due to regular step arrays*

pattern has broad maxima due to the finite terrace width. The infinite periodic arrangement of terraces yields an intensity pattern of δ-functions (centre part of fig. 2.12). This array of scatterers has an inclination angle α with a single terrace. Therefore, the zeroth order beam of this intensity pattern is found at 2α. Since the crystal can be described by a convolution of a single terrace with its periodic arrangement (see also section 2.2.6), the diffraction pattern of the stepped surface according to the convolution theorem is given by the product of the two corresponding patterns. The pattern consists of single and double spots (lower part of fig. 2.12).

The existence of single and double spots can also be easily derived by using the reciprocal lattice and the Ewald construction. In case of a flat surface the spots are sharp and single

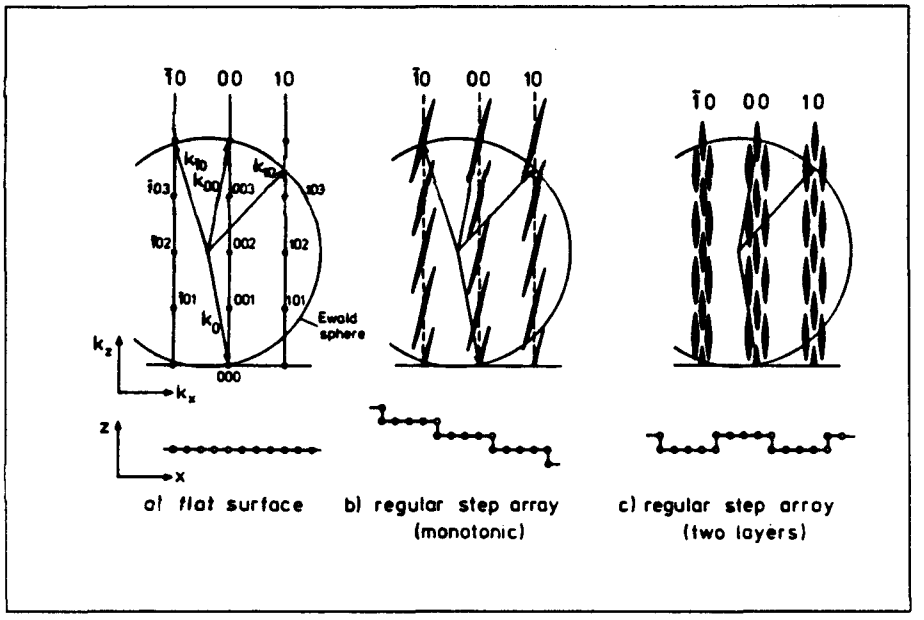

Figure 2.13: *Reciprocal space with Ewald sphere for three forms of surfaces*

for all energies. In fig. 2.13.b the situation is given for the treated example in fig. 2.12. The regular array of steps yields sharp reciprocal lattice rods normal to the macroscopic surface, which intersect the reciprocal lattice rods, due to a single terrace, at reciprocal lattice points originating from the bulk. In fig. 2.13.b the convolution of the two intensity patterns is given. Whether a spot is single or not can be deducted by constructing the Ewald sphere for the concerned energy. The positions at the reciprocal lattice rods, due to a single terrace, where single spots occur correspond to reciprocal lattice points. In fig. 2.13.c a regular array restricted to two atomic layers is treated. The interference function is now composed of three structure factors [LAG82]. One corresponding to the periodicity of the unit consisting of a high and a low terrace separated by a step. With an infinite number of units the reciprocal rods become δ-functions separated by a distance corresponding to the unitsize. The second factor is due to the diffraction of a single finite terrace and therefore has broad maxima. The last factor is accounting for the interference between emergent waves from a high and a low terrace and gives rise to a modulation of the interference function along the reciprocal rods.

Up till now only regular step arrays have been considered. Many irregularities may be described as irregular step arrays. For example, due to a random attack during etching or sputtering, a surface with a certain number of random distributed steps is always formed. For a rough prediction of the LEED pattern the surface is treated as if it is composed of areas with regular step arrays. Then the intensity functions of the regular portions can be added. A few examples of LEED patterns from irregular step arrays are given in fig. 2.14.

Again the single spots at reciprocal lattice points are not affected. The double spots however, reflect all terrace widths by varying splitting. In fig. 2.14.a may be seen that, in case of a surface with both terrace width and step direction irregular, with increasing energy all spots vary between sharp and diffuse spots periodically.

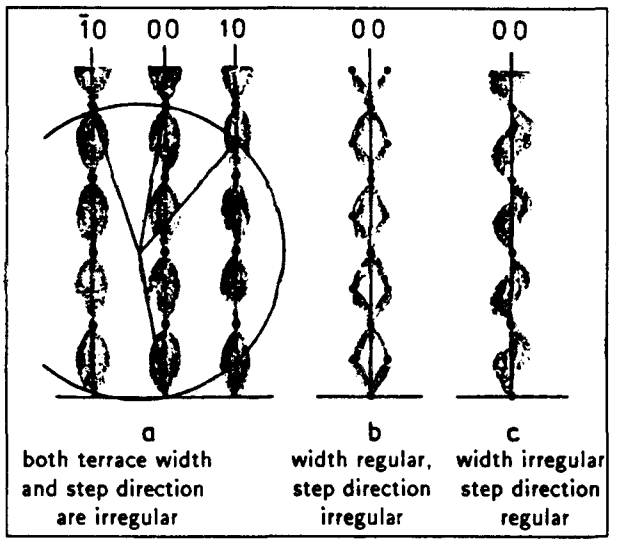

Figure 2.14: *Reciprocal space for three arrangements with irregular step arrays*

In all cases the spot shape at reciprocal lattice points is not affected, due to in-phase scattering of the terraces. Therefore it is important to know in advantage the characteristic energies at which in-phase scattering occur. A general derivation for all reflections and for all faces is given below [HEN70]. The lattice vectors parallel to the surface are given by $\vec{a}$ and $\vec{b}$ and $\vec{c}$ is an arbitrary vector normal to the surface. The reflection (hk) is observed in the direction $\vec{k}$:

$$\vec{k} = \vec{k}_0 + h\vec{a}^* + k\vec{b}^* + L\vec{c}^* \tag{2.33}$$

where h and k are integers and L is arbitrary.
Eq. 2.33 is illustrated in fig. 2.15. Keeping in mind that only elastical scattering at surface atoms is taken into consideration (eq. 2.3), an expression for L can be found in case of normal incidence:

$$L|\vec{c}^*| = |\vec{k}_0| + [|\vec{k}_0|^2 - |h\vec{a}^* + k\vec{b}^*|^2]^{\frac{1}{2}} \tag{2.34}$$

Supposing that the layer distance is given by step height d the step vector $\vec{g}$ can be represented by:

$$\vec{g} = x\vec{a} + y\vec{b} + d\frac{\vec{c}}{|\vec{c}|} \tag{2.35}$$

The values for x and y must be chosen so, that the atomic positions of the surface atoms of all subsequent layers can be described by adding up integer multiples of the vectors $\vec{a}$, $\vec{b}$ and $\vec{g}$. The in-phase condition is satisfied when the phase factor $\exp[i(\vec{k} - \vec{k}_0) \cdot \vec{g}]$ is equal to 1. This leads to the condition:

$$\vec{g} \cdot (h\vec{a}^* + k\vec{b}^* + L\vec{c}^*) = 2\pi S \tag{2.36}$$

with S is an integer. The anti-phase condition is met when S is an integer and a half.
The characteristic or sharp energies can be found by extracting an expression for $\vec{k}$ with help of eq. 2.34, 2.35 and 2.36 and using $E = \frac{\hbar^2 k^2}{2m}$:

$$E_{hk} = \frac{1.504}{4d^2}\left\{S - (hx + ky) + \frac{|h\vec{a}^* + k\vec{b}^*|^2 d^2}{4\pi^2[S - (hx + ky)]}\right\}^2 \tag{2.37}$$

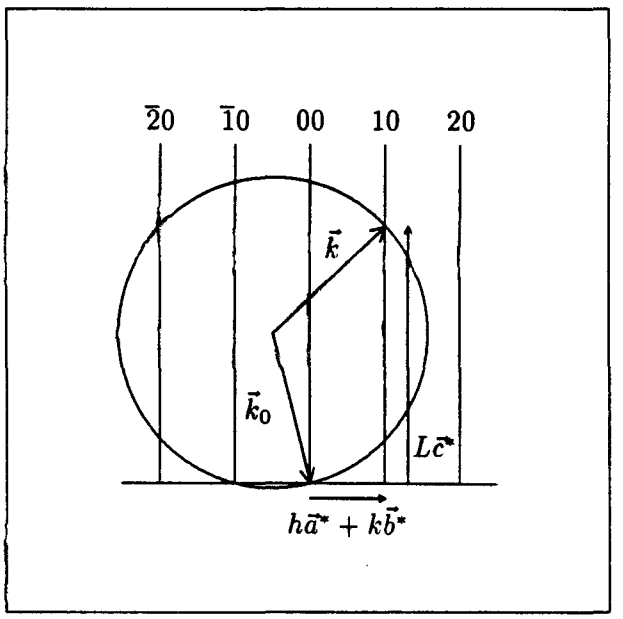

Figure 2.15: *Illustration of the calculation of sharp energies*

with:

$$S \geq \frac{|h\vec{a}^* + k\vec{b}^*|d}{2\pi} + hx + ky \tag{2.38}$$

where E is given in eV and d in nm. In eq. 2.37 no correction should be made for the inner potential, because only scattering at surface atoms of the terraces is considered. In [CLA84] formulae concerning the sharp energies are given, which incorrectly contain the inner potential. For the specular reflection ($h = k = 0$) eq. 2.37 can be very simplified:

$$E_{00} = \frac{1.504}{4d^2} S^2 \tag{2.39}$$

The step height d can be derived from measurements of succeeding sharp energies.

Note that in fig. 2.14 in fact the interference function $|G(\vec{K})|^2$ versus the energy is given, because the interference function determines the shape of a spot. The spot intensity profile is determined by the structure factor $F(\vec{k}_0, \vec{k})$. In fig. 2.16 the spot intensity profiles for a randomly stepped surface are given for different energies (see also fig. 2.10). For the specular reflection ($h = k = 0$) condition 2.36 turns into:

$$L|\vec{c}^*|d = K_\perp d = 2\pi S \tag{2.40}$$

The spot profile consists of two contributions. A sharp reflection, due to the ordered lattice, and a diffuse part, arising from the fluctuation of the scattering amplitude along the surface. The intensity of a spot profile is given by [MOR87]:

$$I(\vec{k}_0, \vec{k}) = \left| \sum_{n=1}^{N} \overline{F}(\vec{k}_0, \vec{k}) \exp[i\vec{K} \cdot \vec{r}_n] \right|^2$$

$$+ \sum_{n=1}^{N} \sum_{m=1}^{N} [(F_n(\vec{k}_0, \vec{k}) - \overline{F}(\vec{k}_0, \vec{k}))((F_m^*(\vec{k}_0, \vec{k}) - \overline{F}^*(\vec{k}_0, \vec{k}))] \exp[i\vec{K} \cdot (\vec{r}_n - \vec{r}_m)] \tag{2.41}$$

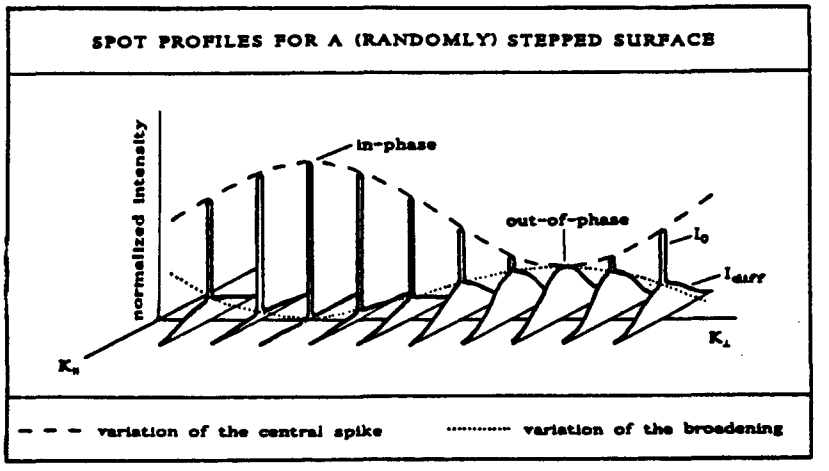

Figure 2.16: *Observed profiles of electron diffraction spots for a randomly stepped surface. Steps at the surface produce a splitting of the spot into a central spike and a broadening. Due to the interference of the electron waves both contributions to the spot intensity vary with vertical component of the scattering vector $K_\perp$ in anti-phase. At the in-phase condition only the central spike occurs, while at the out-phase condition the broadening gets its maximum.*

where $\vec{r}_n$ is a two-dimensional lattice vector, N is the number of unit cells, $\vec{k}_0$ and $\vec{k}$ are the wavevectors of respectively the incoming and outgoing waves and $F_n(\vec{k}_0, \vec{k})$ are the structure factors of the unit cell column values. $\overline{F}(\vec{k}_0, \vec{k})$ is the spatial average of structure factors. The sharp reflection is given by the first summation in eq. 2.41. The diffuse intensity is described by the double sum in eq. 2.41. The sharp reflection has the shape of a Gaussian [WOL89]. The diffuse shoulder has a Lorentzian shape, when the terrace width distribution can be described by the geometric distribution. When there is no interaction between steps, the terrace width distribution is given by the geometric distribution [LU82]:

$$P(N) = (1-\gamma)^{N-1}\gamma \tag{2.42}$$

where $(1-\gamma)^{N-1}$ is the probability of meeting no step passing $(N-1)$ lattice sites and γ is the probability of meeting a step in going from the $(N-1)^{th}$ site to the N^{th} site. The product of $(1-\gamma)^{N-1}$ and γ therefore defines the probability of terraces of width $N\vec{a}$, where $\vec{a}$ is the lattice constant in the considered direction. The average terrace width in the case of the geometric distribution is $|\vec{a}|/\gamma$. Geometric distributions occur in many random, natural grown processes.

When in-phase scattering from equivalent terraces occurs (S is an integer), the scattering mechanism is insensitive to steps and the diffuse part vanishes. The diffraction is maximally sensitive to steps for the out-phase condition (S is an integer and a half). The full width at half maximum of the diffuse intensity is then related to the average terrace size. From an analysis of the angular beam profiles the terrace size distribution can be obtained [BUS86, MOR87].

A distinction should be made between scattering from equivalent and non-equivalent terraces. Non-equivalent terraces differ in effective scattering properties and therefore an extra phase factor $\Delta\phi$ should be included in the scattering factor and condition 2.40 becomes:

$$K_\perp d + \Delta\phi = 2\pi S \tag{2.43}$$

In [MOR87] the angular beam profiles from surfaces with non-equivalent terraces are qualitatively described.

2.2.6 Quantitative information from diffraction patterns

The maximum information available from a diffraction experiment in which intensities are measured and not the phases of amplitudes is the autocorrelation or pair distribution function $\Phi(r)$. This function gives the probability that simultaneously there is an atom at the origin and at the position $\vec{R}$. Consider a one-dimensional surface with lattice constant $\vec{a}$. For this surface the lattice factor G yields:

$$G = \sum_{n=0}^{N} \exp[i\vec{K} \cdot n\vec{a}] \tag{2.44}$$

With help of the local density function:

$$n(\vec{r}) = \sum_{n=0}^{N} \delta(\vec{r} - n\vec{a}) \tag{2.45}$$

eq. 2.44 can be written as:

$$G = \int_{-\infty}^{\infty} n(\vec{r}) \exp[i\vec{K} \cdot \vec{r}] d\vec{r} \tag{2.46}$$

As a result, the intensity is proportional to:

$$\begin{aligned} I \sim |G|^2 &= \int_{-\infty}^{\infty} n(\vec{r}) \exp[i\vec{K} \cdot \vec{r}] d\vec{r} \int_{-\infty}^{\infty} n(\vec{r}') \exp[-i\vec{K} \cdot \vec{r}'] d\vec{r}' \\ &= \int_{-\infty}^{\infty} \int_{-\infty}^{\infty} n(\vec{r}) n(\vec{r}') \exp[i\vec{K} \cdot (\vec{r} - \vec{r}')] d\vec{r} d\vec{r}' \end{aligned} \tag{2.47}$$

Substitution of $\vec{r}' = \vec{r} + \vec{R}$ gets:

$$I = |G|^2 = \int_{-\infty}^{\infty} \Phi(\vec{R}) \exp[i\vec{K} \cdot \vec{R}] d\vec{R} \tag{2.48}$$

where:

$$\Phi(\vec{R}) = \int_{-\infty}^{\infty} n(\vec{r}) n(\vec{r} + \vec{R}) d\vec{r} \tag{2.49}$$

is the autocorrelation function.
From eq. 2.48 can be seen that the intensity I is proportional to the Fourier transform of the autocorrelation function.

Instrumental limitations affect the observed intensity pattern. The major sources for instrument broadening are the incident beam divergence of the electron gun, the energy uncertainty in the incident beam, the incident beam diameter and the detector aperture width. The observed intensity $I_m(\vec{K})$ can be described as a convolution:

$$I_m(\vec{K}) = I(\vec{K}) \star T(\vec{K}) \tag{2.50}$$

where $I(\vec{K})$ is the ideal intensity pattern and $T(\vec{K})$ is the instrumental response function. The Fourier transform of $I(\vec{K})$ is given by the autocorrelation function $\Phi(\vec{x})$. If $t(\vec{x})$ is the Fourier transformed of the instrument response function $T(\vec{K})$, the observed intensity pattern can be approximated by:

$$I_m(\vec{K}) \sim \mathcal{F}\{\Phi(\vec{x}) \cdot t(\vec{x})\} \tag{2.51}$$

In general the function $T(\vec{K})$ is a Gaussian with halfwidth T, so the transfer function $t(\vec{x})$ has an halfwidth $t \sim \frac{1}{T}$, the transfer width. The instrument response reduces correlation over distances beyond the transfer width so that fine structures in the profile are smoothed out. The necessary steps for a quantitative analysis of a diffraction profile are shown in

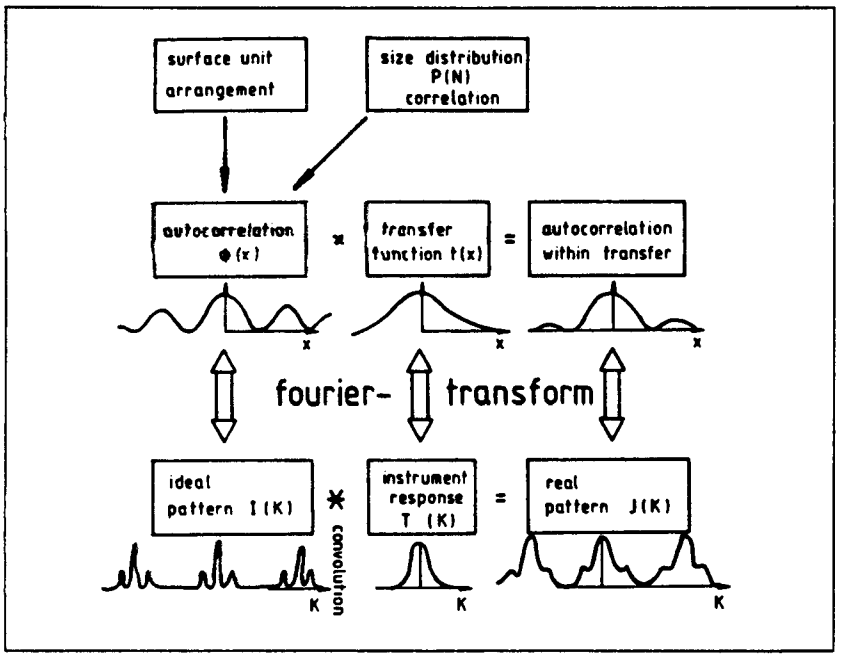

Figure 2.17: *Scheme for the evaluation of diffraction patterns*

fig. 2.17. First the spot profile $J(K_x)$ or $J(K_x, K_y)$ is recorded. With help of the instrument response function $T(\vec{K})$, the ideal pattern $I(K_x)$ or $I(K_x, K_y)$ is calculated. The Fourier transform yields the autocorrelation function. The terrace size distribution is obtained by fitting with model calculations. The actual surface atom arrangement cannot be derived, because the phase of the diffraction pattern has not been measured. The final result is the size distribution of the defects as an average over the illuminated part of the surface.

2.3 The SPA-LEED apparatus

The SPA-LEED apparatus is designed by Henzler's group [SCH86]. The instrument is produced by Leybold-Heraeus GMBH in Köln. In fig. 2.18 the most important parts of the instrument are represented. The instrument can be used in two modes; the viewing mode and the channeltron mode. The screen serves for the visual inspection of the LEED pattern. It consists of a glass plate covered with a thin transparant metal layer and a UHV compatible phosphor. By a high voltage of 5 kV the diffracted electrons are accelerated to the plate and

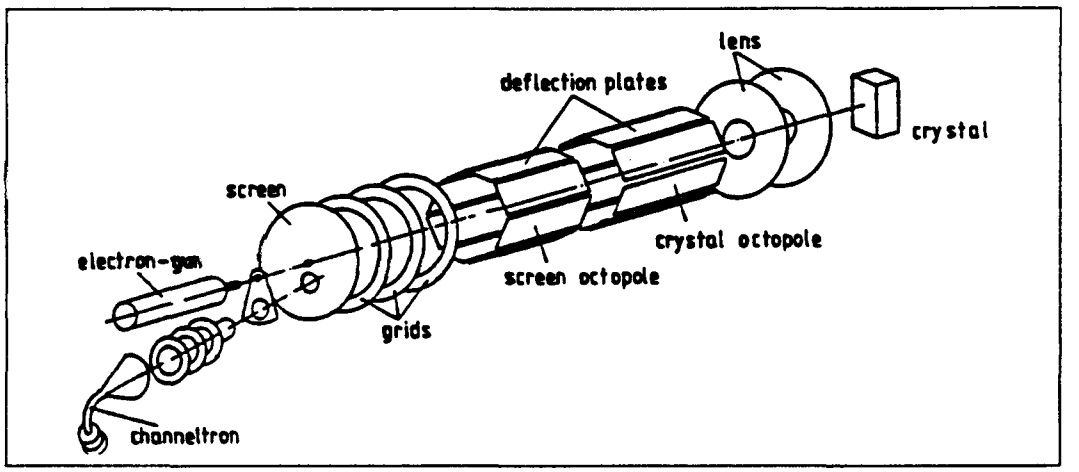

Figure 2.18: *Scheme of the SPA-LEED system*

thus excite phosphorescence at their point of incidence. A repeller net in front of the screen is used for suppression of inelastically scattered electrons. In the viewing mode, electrons can be detected which leave the sample at maximum angle of 10.5 degrees with respect to the axis of the system.

In the screen two holes are made, one for the electron gun and one for the channeltron. The high dynamic range of the channeltron detector (10^6) allows an accurate measurement of the spot and background intensities. The electron gun and detector are aligned in a fixed geometry. The axes of the electron gun and the detection system form an angle of 7.5 degrees and meet in a point 15 mm in front of the instrument, where the sample surface should be placed. The diffracted electrons enter the channeltron housing through an aperture of 100 μm diameter. This means an effective opening angle of 0.023° with respect to the sample surface. The diffraction pattern is scanned over the channeltron aperture by means of applying voltages on the octopoles of the deflection units (fig. 2.19). Note that the angle between incident and

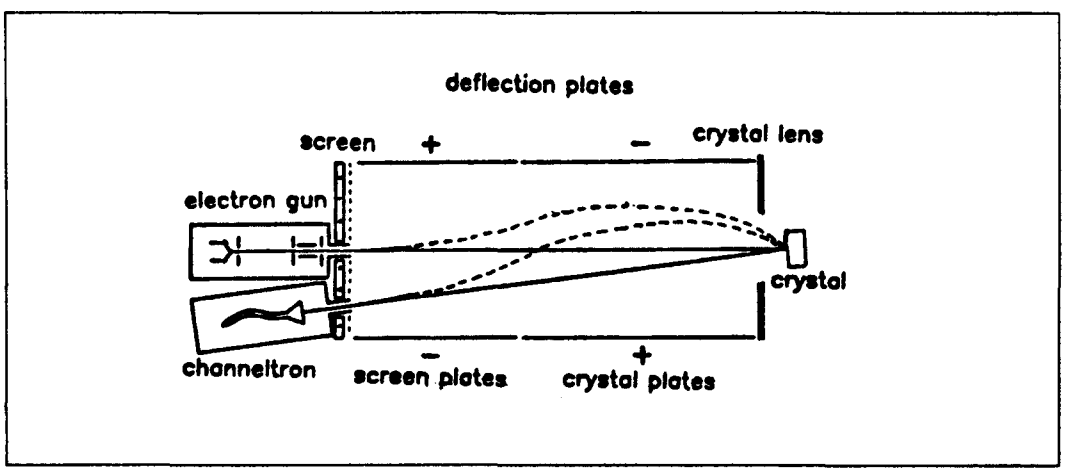

Figure 2.19: *The deflection unit:*
— :trajectory of electrons with no deflection voltages applied
__ :trajectory of electrons with deflection voltages applied

emergent waves on the crystal remains constant. This constant angle, fixed at 7.5 degrees, yields the modified Ewald construction for SPA-LEED, shown in fig. 2.4.b.

The applied deflection voltages to move the pattern across the channeltron aperture are proportional to the shift $\Delta k_{||}$ made in reciprocal space:

$$\Delta U = S\Delta k_{||} \tag{2.52}$$

where S is called the deflection sensitivity. This sensitivity is proportional to the square root of the electron energy:

$$S = (2.76 \pm 0.05)\sqrt{E} \quad \text{VÅ(eV)}^{-\frac{1}{2}} \tag{2.53}$$

This proportionality has been verified using a Ni(311)-sample.

The diameter of the analysis spot, formed by the electron beam at the sample surface, varies slightly as a function of electron energy (fig. 2.20).

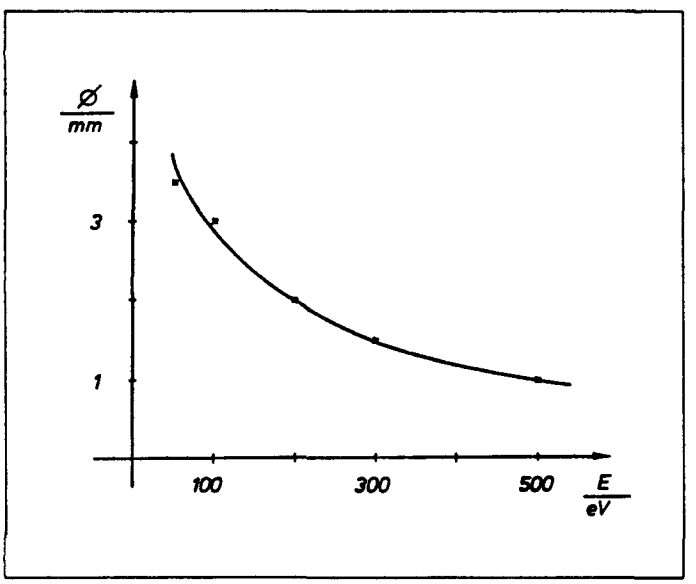

Figure 2.20: *Diameter of the analysis spot as a function of electron energy*

The channeltron is controlled with a Data Aquisition Unit, which in turn is connected with a HP 9000-350 system. The different experiments are controlled by a special designed program. Possible experiments are area scans, profile scans, line scans. Line scans can be made with a point detector or a slit detector, which are in fact two different measurements. For example, the measured intensities in x-direction are respectively for a point detector and a slit detector:

$$I_1(K_x, 0) \quad \text{and} \quad I_2(K_x) = \int I(K_x, K_y) dK_y \tag{2.54}$$

The terrace width distribution $P_1(N)$ and $P_2(N)$ as derived from the functions I_1 and I_2 by fitting have a different meaning. $P_1(N)$ is the width distribution derived by projecting the whole surface onto the x-axis and treating that composite arrangement as system for (coherent) diffraction. $P_2(N)$ is obtained by treating the atomic rows in x-direction independently and summing the probabilities of all rows (incoherent superposition).

In order to avoid the application of large deflection voltages, the sample is mounted to a sample manipulator, which can rotate the sample around the axis perpendicular to the plane

through the axes of the electron gun and the detection system. The design of the manipulator is based on a patent of Philips and is constructed at the Eindhoven university of technology. In fig. 2.21 two photos of the manipulator are shown. The sample is rotated by stirring the wheel at top of the manipulator. The rotation is transmitted by means of a wobbling disk mechanism to the sample holder at the bottom of the manipulator. The rotation angle can directly be read from the inscribed scale at the sample holder, with an accuracy of 0.05 degrees. A second rotation around the normal of the sample surface is under construction.

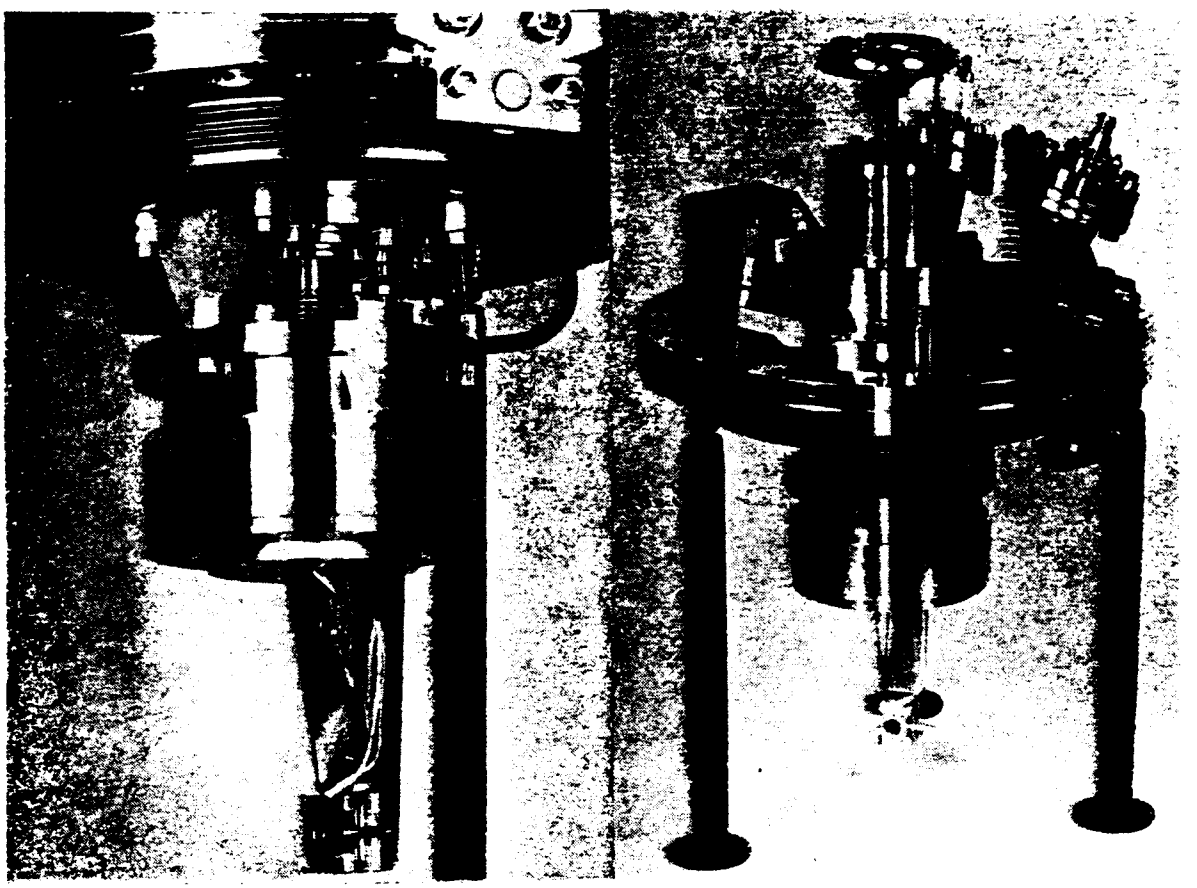

Figure 2.21: *The manipulator*

Chapter 3

Surface topography of pyrolytic graphite

The SPA-LEED experiments on the surface of highly oriented pyrolytic graphite are summarized in this chapter by means of a preprint. In subsection 3.2 some extra reflections are included.

3.1 Surface topography of pyrolytic graphite

SURFACE TOPOGRAPHY OF PYROLYTIC GRAPHITE

A.G. ROOSENBRAND, M.W.C. VAN BECKHOVEN AND H.H. BRONGERSMA

Department of Physics
Eindhoven University of Technology
Den Dolech 2, P.O. Box 513, 5600 MB Eindhoven, The Netherlands

It is demonstrated that highly oriented pyrolytic graphite (HOPG) samples show a wide spread in out of plane orientations of the crystallites at the surface.This may cause asymmetric features in scanning tunneling microscopy images. These misorientations and not the crystallite size determine the widths of the observed diffraction rings. The measurements on HOPG have been performed with a high resolution spot profile low-energy electron diffraction system (SPA-LEED). The results of SPA-LEED and STM are found to be complementary.

INTRODUCTION

Defects at solid surfaces can influence many properties such as nucleation, adsorption, density of states, catalytic activity and Hall mobility. Surface topology describes the imperfections

at the solid vacuum interface. Examples of topological phenomena are facets, steps and terraces, islands, domains, mosaic structures, surface roughening and surface melting. Several techniques can be used to study surface defects. One of them is the scanning tunneling microscopy (STM). This technique provides information about the local (in space and energy) density of states [1]. The area scanned by a tunneling microscope is approximately 100 × 100 nm^2. Another method suitable for the study of surface defects is the recently developed [2] high resolution spot profile analysis low-energy electron diffraction (SPA-LEED) system. In diffraction experiments one operates in reciprocal space. So the angular intensity distribution within a single spot reveals diffraction effects originating from topological features at the sample surface. The sample area probed by the SPA-LEED apparatus is typically 10 mm^2.

In this work measurements are presented obtained with SPA-LEED. The sample under study was highly oriented pyrolytic graphite (HOPG) as described in [3]. HOPG can be used as a calibration standard for the inplane X and Y axes of an STM [4], because the surface of HOPG has translational symmetry over a range of hundreds of lattice constants.

For comparing SPA-LEED and STM we performed an experiment on HOPG with the former technique. Our aim is to compare and to contrast the possibilities of the two techniques. It is intended to contribute to the understanding in which way STM and SPA-LEED are competing and how they can be complementary as well.

STM images on HOPG should reveal the honeycomb structure of the graphite lattice. This structure has a threefold symmetry. Indeed, such patterns have been found [1,5,6,7]. The dominant feature in these images is the hollow in the middle of the carbon hexagon. Carbon atoms with neighbours in the second layer appear as small peaks, the ones without as saddle points [1]. STM images with varying degrees of asymmetry have been found [4]. This might be due to an asymmetric tip [1,4] or to a tilted sample [4].

LEED experiments on natural graphite show a threefold symmetric pattern for the (0001) surface [8]. This indicates that one of the two possible surface terminations is dominant. Experiments on HOPG do not show a hexagonal LEED pattern, but a ring shaped structure for the first and higher order reflections [9,15]. This is indicative for a random orientation of many small crystallites within the surface plane [10].

EXPERIMENT

The experiments were performed using a commercially high-resolution spot profile analysis LEED system (Leybold-Heraeus), which allows the recording of diffraction features by scanning the diffracted beam over a channeltron with a small circular aperture by using electrostatic deflection. The instrument is described in [2]. The SPA-LEED system is mounted to an UHV-vessel. This chamber contains a μ-metal shielding to reduce the effect of stray-magnetic fields. The remaining field was smaller than 10 nT.

For easy data acquisition and data manipulation a link has been made to a workstation (HP 9000-350 system). To control the experiment an user friendly menu program has been developed. From an area scan, as shown in fig. 1, a spot profile can be obtained by simple data manipulation. By adding the appropriate channels in an area scan one can simulate any desired detector shape, for instance a slit. By using the workstation data can be presented in full colour on a graphics terminal and a colour printer.

Since a graphite surface is very inert to the adsorption of gases fresh surfaces can be obtained by cleaving the sample with Scotch tape even in air [11]. After cleaving the sample was immediately transferred via an airlock into the specimen chamber with a base pressure

lower than $5 \cdot 10^{-8}$ Pa. The sample was mounted in a very stable newly developed target manipulator. A rotational accuracy of 0.05° is easily obtained [12]. Stability is necessary

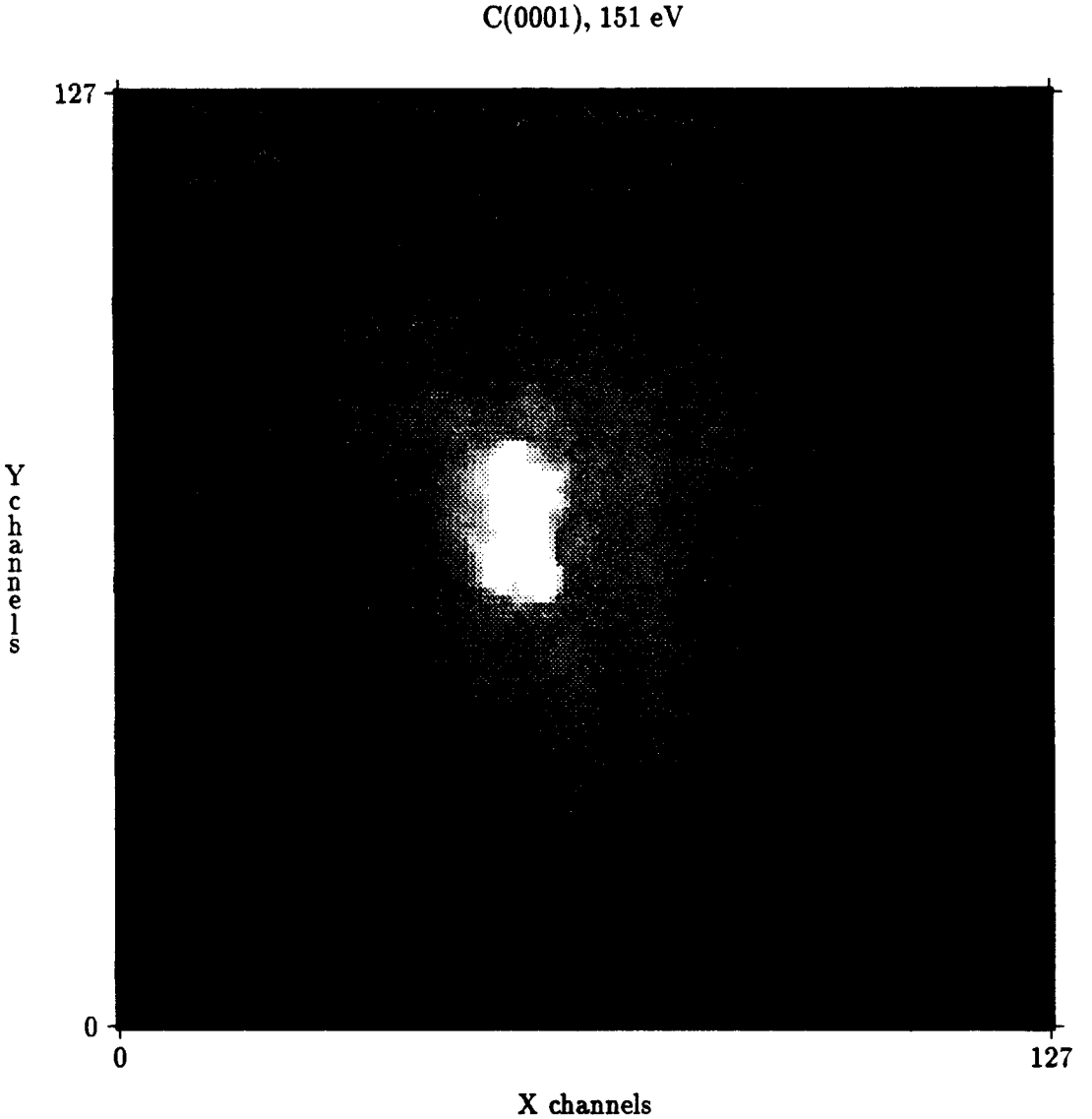

Figure 1: *Area scan of specular reflection showing different maxima*

for the scanning procedure used for data acquisition.

RESULTS

The measurements were made after a heat treatment of the HOPG sample at about 900 K for one hour. In fig. 1 an area scan of the direct reflection is presented. This reflection clearly consists of several spots. From fig. 2 it will be clear that the first order reflections form a ring. As can be seen there are occasional bright spots in the ring. The higher order reflections were measured after rotating the sample in such a way that the diffracted beams hit the detector.

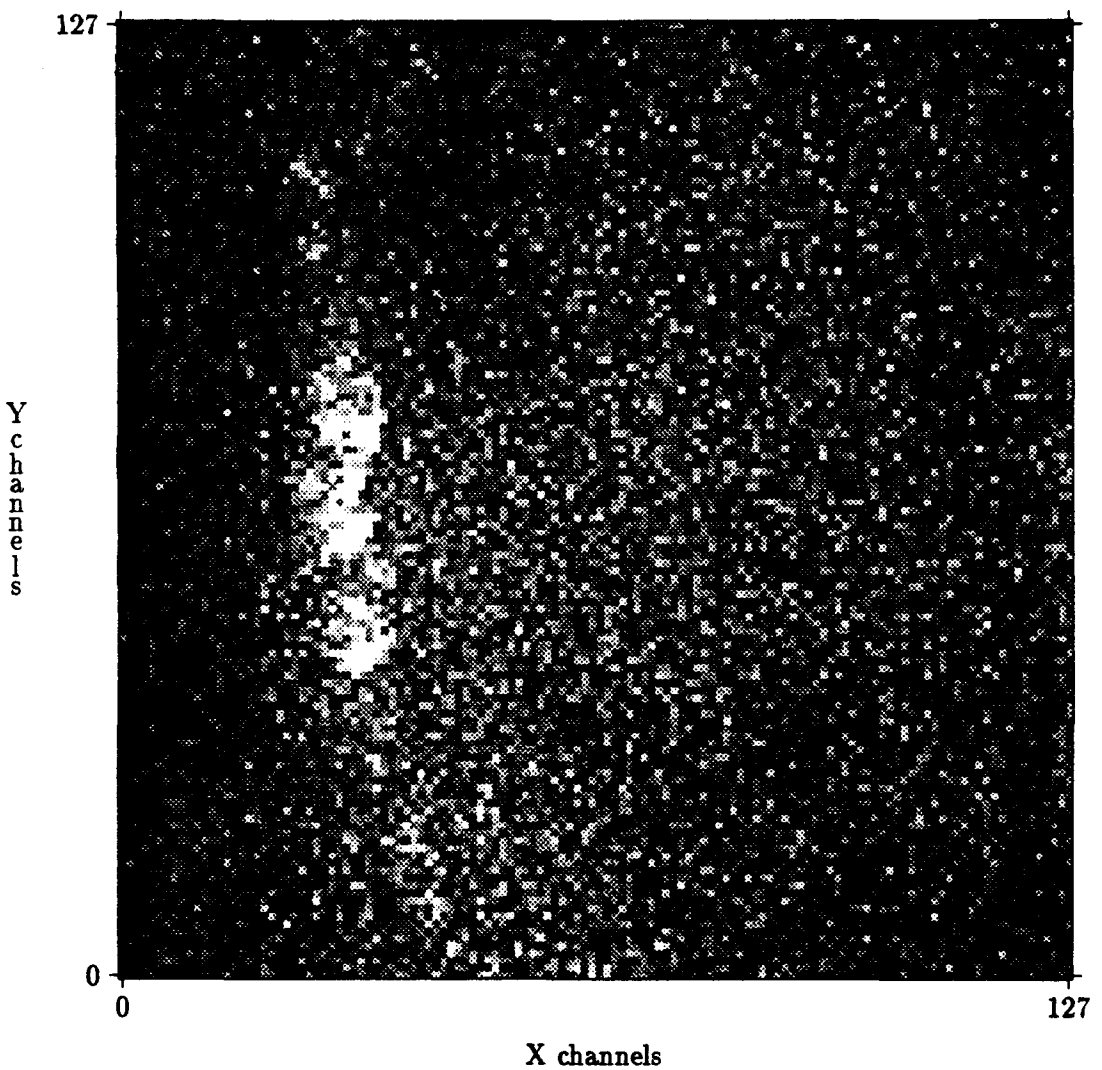

Figure 2: *Part of first order ring at the left of the specular reflection*

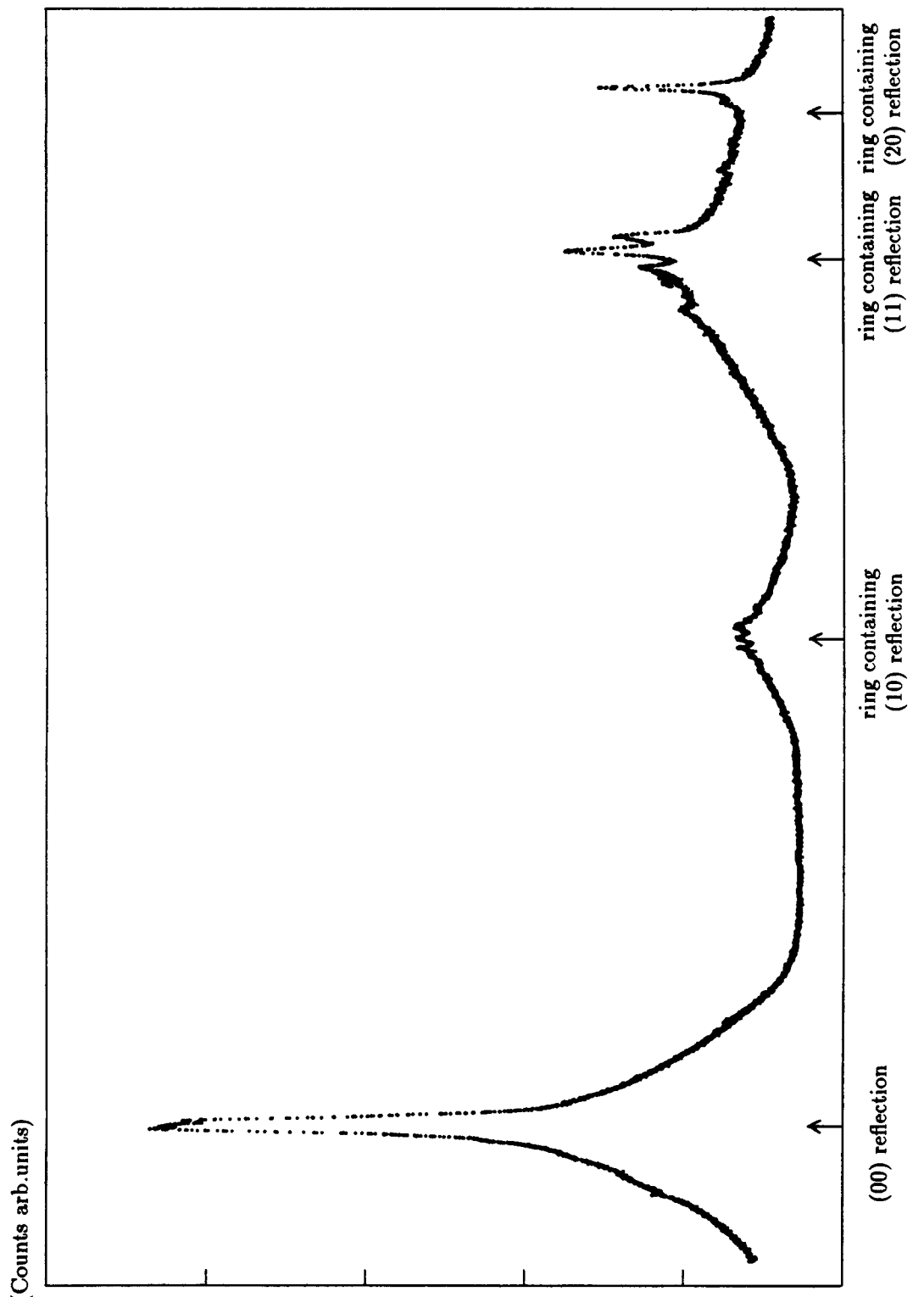

Figure 3: *Line scan of graphite starting at the specular reflection intersecting the subsequent rings*

Consequently, large scanning voltages are not needed.

In fig. 3 a composition of five line scans is given starting at the centre of the direct reflection and passing through the subsequent rings. The arrows indicate the direct reflection and the expected positions for the rings containing respectively the (10), (11) and the (20) reflection. Each ring shows peak separations corresponding to an angular spread in the range of $0.3° - 0.5°$.

Only for the specular reflection it is possible to obtain an I-V-curve with the SPA-LEED system at which the angle of incidence is constant ($\beta = 3.75°$). The obtained intensity profile closely resembles the peak locations as observed previously on natural graphite [13] and on pyrolytic graphite [14].

CONCLUSIONS

From the existence of several intensity maxima in the direct reflection, as shown in fig. 1, it is concluded that HOPG has a mosaic structure in agreement with the interpretation given in [10]. The orientations out of the macroscopic sample plane are typically a few tenths of a degree. This kind of spread is well known to occur in HOPG [3]. However, out of plane orientations of several degrees do occur, as can be deduced from fig. 3. This large spread is probably induced by the cleaving process. Since different angular spreads were found after each cleaving process. A reflection is composed of a large number of rather narrow peaks, as compared to the total width. Every peak corresponds to a certain orientation of a crystallite in the surface. Its width is inversely proportional to the range of translation symmetry in the crystallite surface. This range is about 100 nm [1,4], which equals the transfer width of the SPA-LEED system. The background between the zero and higher order reflections is attributed to random effects in the sample surface.

The rings show the same range of misorientations as observed in the specular reflection. Therefore it is concluded that, in contradiction to what is stated in [9], the width of the ring is not a measure of the average size of the crystallites. It merely contains information about the angular spread of the numerous out of plane orientations in the mosaic structure.

The observation of the distribution over rings of the first and higher order reflections leads to the conclusion that the crystallites are rotated rather randomly with respect to one another. Consequently the reciprocal lattice rods form coaxial cylinders around the (00) rod in reciprocal space. Occasionally intensity maxima do occur on the ring. These intensity maxima are not caused by dynamic scattering effects. Since the angle between incident and emergent wave vector remains constant using SPA-LEED [2], a modified Ewald construction with centre at the origin has to be used. Therefore the intersections of the cylinders in reciprocal space with the modified Ewald sphere consists of concentric circles. In a conventional LEED system used in [15], the cylinder axis generally will not contain the centre of the Ewald sphere (i.e. $\beta \neq 0°$) and the intersection of the cylinder and the sphere has the shape of an ellipse. Along the ellipse the momentum transfer perpendicular to the surface changes continuously, giving rise to intensity variations [15]. In our case, however, the intensity maxima in the ring indicate some preferential orientations. The same observation has been reported in [9].

The occurrence of misorientations, whether induced by the cleaving procedures or intrinsic to HOPG, may explain part of the observed asymmetries in STM images, since model calculations [4] show that a tilted specimen can cause asymmetric features in a STM image. This in addition to the effect of an asymmetric tip [1].

STM is very suited to study the surface of pyrolytic graphite on an atomic scale. The SPA-LEED is very powerful in determining the distribution of the surface orientations of the crystallites. The combination of the results obtained with both techniques gives a complete picture of the surface topography of HOPG.

REFERENCES

[1] G. Binnig *et al.*, Europhys. Lett. **1** (1986), 31

[2] U. Scheithauer, G. Meyer and M. Henzler, Surf. Sci. **178** (1986), 441

[3] A.W. Moore, in: Chemistry and Physics of Carbon, ed. P.L. Walker, Jr. and P.A. Thrower (Dekker, New York, 1981) **17**, 233

[4] J. Schneir *et al.*, Phys. Rev. B **34** (1986), 4979

[5] H.J. Mamin *et al.*, Phys. Rev. B **34** (1986), 9015

[6] A. Bryant *et al.*, Appl. Phys. Lett. **48** (1986), 832

[7] Van Kempen, private communication

[8] N.J. Wu and A. Ignatiev, Phys. Rev. B **25** (1982), 2983

[9] M.E. Schrader, J. Phys. Chem. **84** (1980), 2774

[10] M.G. Lagally, in: Chemistry and Physics of Solid Surfaces IV, ed. R. Vanselow and R. Howe (Springer-Verlag, Berlin 1982), 281

[11] M.F. Toney *et al.*, Phys. Rev. B **27** (1983), 6413

[12] A.G. Roosenbrand, P. Brinkgreve and H.H. Brongersma, to be published

[13] J.J. Lander and J Morrison, J. Appl. Phys. **35** (1964), 3593

[14] L.H. Germer *et al.*, C. R. Acad. Sc. Paris, t 262 C (1966), 1059

[15] J. Escard, S. Goldsztaub and G. David, C. R. Acad. Sc. Paris, t 262 B (1966), 966

3.2 Comparison of the measured I-V-curve and curves in literature

Only for the specular reflection it is possible to obtain an I-V-curve with the SPA-LEED system at which the angle of incidence is constant ($\beta = 3.75°$). This curve has been measured for the maximum intensity within the specular reflection and for the intensity of the direct reflection integrated over approximately the first Brillouin zone. Since the area scanned by SPA-LEED varies with energy, the observed arrangement of out of plane crystallites also changes with energy. Therefore not only the relative positions of the maxima in the direct reflection will vary as function of energy, but also the absolute maxima of the specular reflection will originate from other crystallites as function of energy. Consequently, the maxima of the specular reflection is not well defined. Therefore the I-V-curve is best obtained from the intensity of the direct reflection integrated over the first Brillouin zone as function of energy. The estimated positions of the curve peaks corresponding to the third Bragg reflection in the I-V-curve are given by (see also eq. 2.39):

$$E = \frac{150.4S^2}{4d^2\cos^2\beta} - |V_{0r}| - \Phi \tag{3.1}$$

where d is the interlayer distance ($d = 3.354$ Å), β is the angle of incidence and V_{0r} is the inner potential. Φ is the contact potential, i.e. the difference $\Phi_k - \Phi_s$, difference in work function between kathode and sample.
The obtained intensity profiles closely resemble the peak locations as observed previously on natural graphite [13] and on pyrolytic graphite [14] (see section 3.1). In fig. 3.1 a comparison with the last one can be made. The arrows in fig. 3.1.a indicate the expected peak positions calculated with eq. 3.1 for $\beta = 0°$, $V_{0r} = -9$ eV and $\Phi = 2$ eV. In this work the I-V-curve has been measured with a constant filament current, in [14] the I-V-curve has been obtained with the sample current set at the constant value of $I_0 = 1.0\,\mu$A. The experimental method of [14] reveals an overall increase of the intensity for decreasing voltages, which will be referred to as 'background'. As a result of this 'background' the range of measured intensities contains several orders of magnitudes. Peaks in fig. 3.1.a can be roughly approximated by the 'background' and a Gaussian peak. For the peak at $E = 71$ eV for $\beta = 4°$ this approximation yields:

$$I(E) = 0.12\exp\left[-\frac{E}{13}\right] + 3.5\cdot 10^{-3}\exp\left[-\left(\frac{E-79.54}{4}\right)^2\right] \tag{3.2}$$

where the first term represents the 'background' and the second term the Gaussian peak. The value of 79.54 eV gives the position of the maximum of the Gaussian peak and has been derived from:

$$\left.\frac{dI(E)}{dE}\right|_{E=71\text{eV}} = 0 \tag{3.3}$$

Correction for the contact potential (2 eV) yields a peak position at $E = 77.54$ eV. The I-V-curve in this work is lacking the 'background' of the approximation, due to the experimental method. Therefore the peak position should be at about 77.54 eV. After correction for the contact potential ($\Phi = 0.5$ eV), the obtained values are 75.1 eV and 76.1 eV for respectively the integrated intensity curve and the maximum intensity curve.

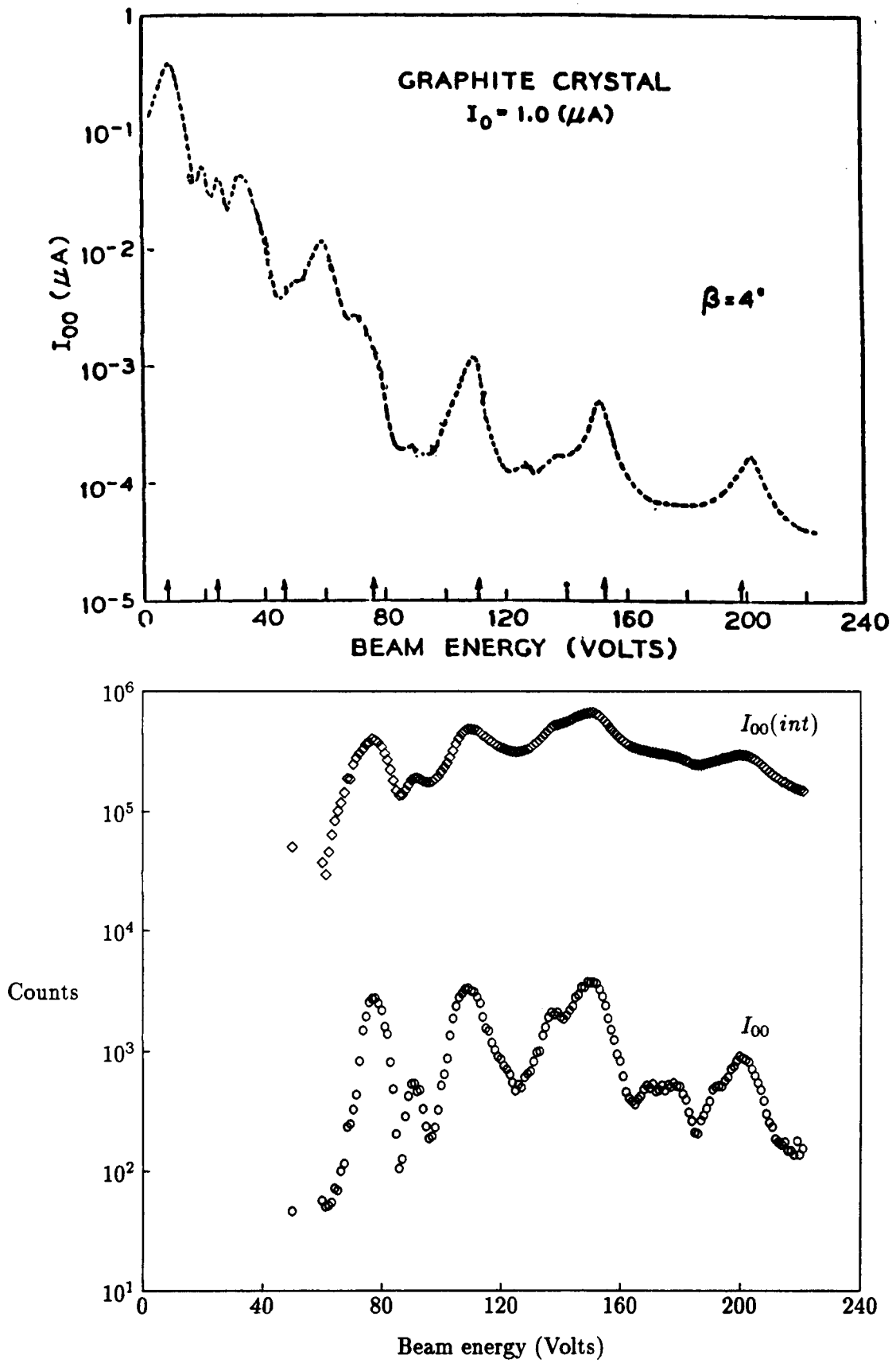

Figure 3.1: *Comparison of the results for the I-V curve from ref.[14] and our work*

In table 1 the measured peak positions are given corrected for the contact potential collected for the $I_{00}(int)$-V-curve and [14].

table 1: *Comparison of the corrected data obtained from [14] and curve 1*

S^2	corrected peak positions (in eV)	
	ref.[14]	this work
25	69	75.1
30.25		90.1
36	108	108.3
49	150	149.5
64	202	199.5

It is clear that for higher voltages the peak positions correspond very well.

From the relation between the peak positions corrected for the contact potential and S^2, the layer distance d and the inner potential V_{0r} can be derived. For respectively [14] and this work the following expressions are obtained:

$$E_{peak} = 3.34S^2 - 9.7 \quad \text{(ref.[14])} \tag{3.4}$$

$$E_{peak} = 3.20S^2 - 6.2 \quad \text{(this work)} \tag{3.5}$$

From the slope of eq. 3.4 a layer distance of 3.36 Å can be calculated and the inner potential is given by -9.7 eV. The layer distance calculated from eq. 3.5 values 3.44 Å and the inner potential is given by -6.2 eV.

Summarizing the results from the comparison of the I-V-curve from ref [14] and the I-V-curve measured in this work the following conclusions can be made. The I-V-curve measured under condition of a constant filament current shows peaks at positions shifted to the right compared to the I-V-curve measured under condition of a constant sample current [14]. These shifts increase for decreasing voltages. As can be seen from fig. 3.1, the intensities in the I-V-curve show an overall increase with decreasing voltages for the data of [14], which is not observed in our work. This is considered to be the main cause for the peak shift. This suggestion is supported by the fact that for increasing voltages the peak positions of [14] and this work are comparable. A rough correction for this shift reveals the peak at $E = 71$ eV in [14] shift to $E = 77.5$ eV, which decribes fairly well the measured values of 75.1 eV and 76.1 eV in this work. The relation between peak position and S^2 reveals good values for layer distance and inner potential for the data collected from [14]. For this work the obtained relation has a discrepancy, due to the incorrect measuring method.

Chapter 4

Experiments on Galliumarsenide

The defect structure of semiconductor surfaces has recently come under intensive study [LAR81,CHA82,SAU89,WEI89]. In particular, the appearance and geometric distribution of steps, their height and reconstruction are investigated. In this chapter the results of SPA-LEED experiments on the (001) surface of GaAs will be presented and discussed.

4.1 Description of GaAs(001)

GaAs has a zincblende structure (fig. 4.1). A zincblende structure consists of two interpene-

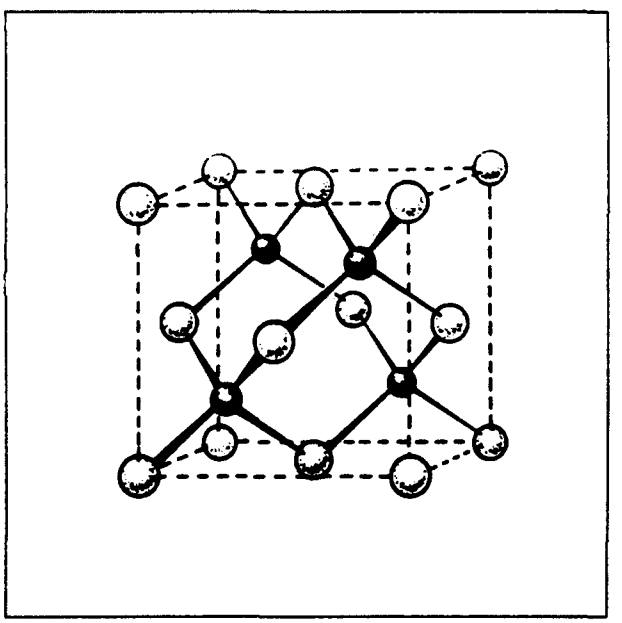

Figure 4.1: *GaAs*

trating face-centered cubic (FCC) Bravais lattices, each composed of either Ga atoms or As atoms. The two FCC lattices are displaced along the body diagonal of the cubic cell by one quarter the length of the diagonal. So the translation vector between the two sublattices is given by:

$$\vec{d} = \frac{a_0}{4}(\vec{e}_x + \vec{e}_y + \vec{e}_z) \tag{4.1}$$

where a_0 is the length of the edge of a face centered cube, for GaAs a_0 equals 5.65315 Å [WEA87].

The (001) surface of GaAs consists solely of one kind of atoms and is therefore called a polar surface. In fig. 4.2 the unit cell of the unreconstructed (001) surface of GaAs is presented, where $\vec{a}$ and $\vec{b}$ are the lattice vectors and a_0 is the length of a face-centered cube side. The atoms are equally spaced on the (001) surface and every atom has two bonds to the layer above and below. Consequently, the unrelaxed surface atoms have two back bonds and two unsaturated dangling bonds. This is not the most stable configuration, which is demonstrated by the large variety of surface reconstructions that exists.

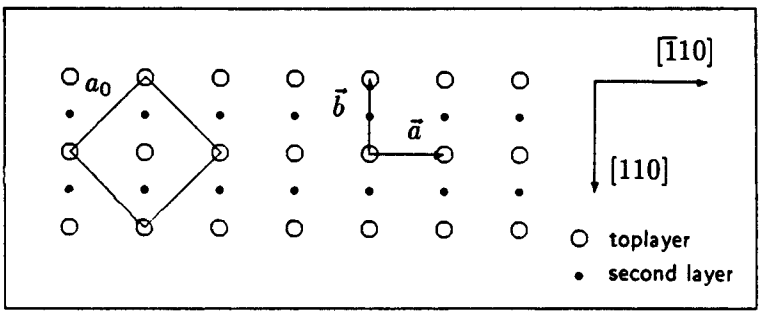

Figure 4.2: *Schematic view of the ideal GaAs(001) surface*

4.1.1 Reconstructions on GaAs(001)

For {001} surfaces many reconstructions have been observed, distinguished in As-stable and Ga-stable reconstructions. Reconstructions with a preponderance of As atoms in the outermost layer are (2×4), c(4×4) and c(2×8), while (4×1), (4×2), (4×6) and c(8×2) are reconstructions produced when Ga atoms are in excess [LAR81,BAC81,DAW82]. In this subsection models are presented for the As-stable reconstructions.

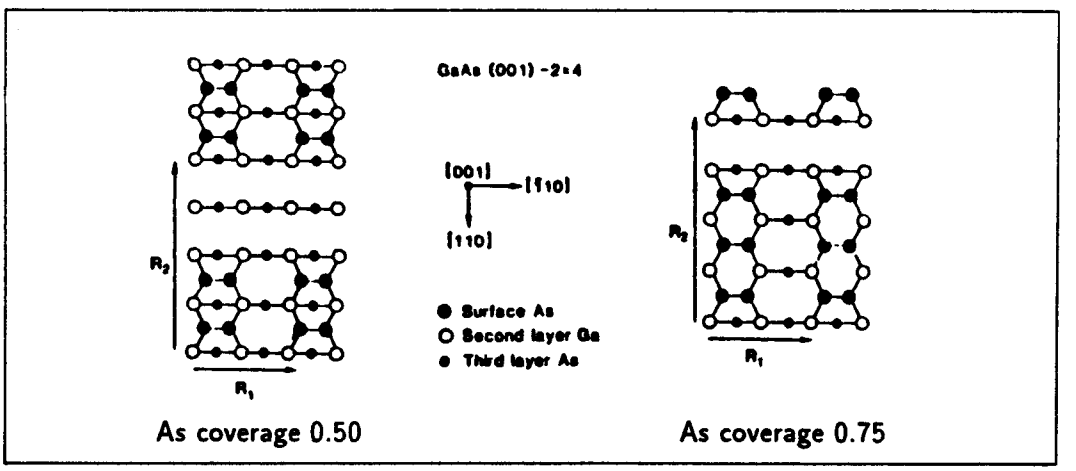

Figure 4.3: *Possible arrangements for (2×4) reconstruction, based on the vacancy model*

First the (2×4) reconstruction will be discussed. Generally is agreed that the (2 × 4) reconstruction is As-stabilised. Up till now it has not been possible to relate it to any specific

surface composition [LAR88]. The surface reconstructs with a twofold periodicity along the [$\bar{1}$10] direction. It is therefore assumed that the arsenic atoms pair up to dimers in this direction. The problem has always been to determine the arrangement of these dimers, which results in a fourfold periodicity along the [110] direction. Recently [LAR88, PAS88], a vacancy model has been proposed in which the fourfold periodicity in the [110] direction is due to a regular array of missing arsenic dimers (fig. 4.3). In this figure two possible arrangements are given (As coverage 0.50 and 0.75) of missing rows of arsenic dimers revealing the (2×4) reconstruction. This is in agreement with experimental evidence for a variable range of stoichiometries (i.e., As coverage) for the (2×4) surface reconstruction. STM images provide evidence for this model [PAS88]. Furthermore, STM images show that the (2×4) units may

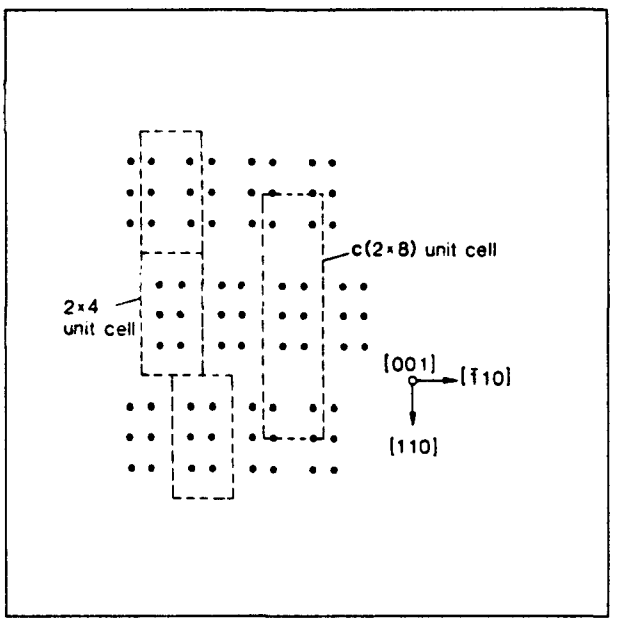

Figure 4.4: *Construction of c(2×8) by domain formation in the vacancy model*

be arranged so as to give small domains of either (2×4) or c(2×8) reconstructions. In the (2×4) models the positions of the As-As dimers on either side of the missing row(s) of As atoms in the uppermost layer do not shift. If the position of the dimers on either side of the missing row(s) is shifted, the structure c(2×8) occurs, as shown in fig. 4.4.

The only theoretical model for the c(4×4) reconstruction is supposed to have an equal amount of symmetric and asymmetric dimers [CHA82]. However, experimentally no asymmetric dimer bond bands have been found [LAR83]. In [LAR83], the suggestion is made that models for the c(4×4) structure should be derived from an As-terminated surface on which additional As is chemisorbed, including features representative of amorphous As. Therefore, the As-As bonding would ideally be trigonal. Fig. 4.5 shows possible arrangements of the overlayer As atoms, for different overlayer coverages. Experimental observations provide evidence for the maintenance of the reconstruction for variable As coverages.

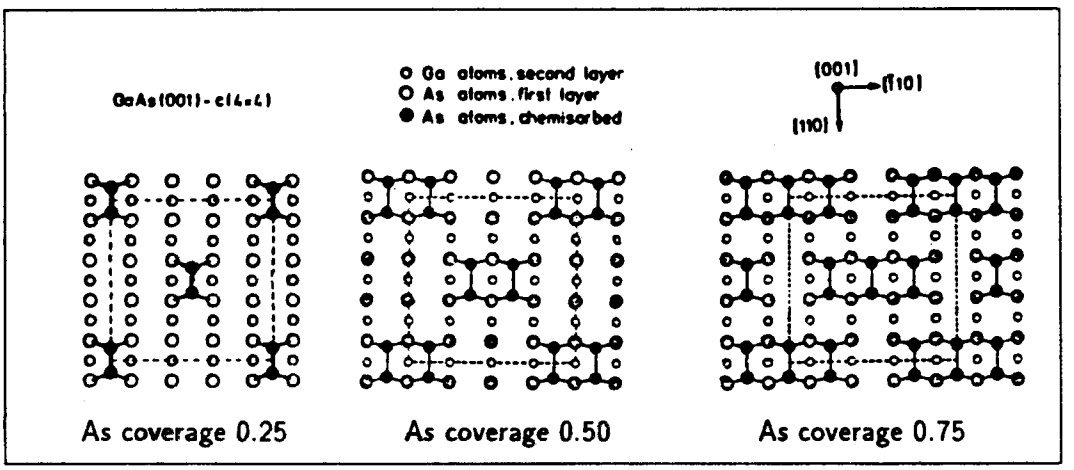

Figure 4.5: *Possible models for the c(4×4) surface*

4.1.2 LEED patterns for the reconstructed GaAs(001) surface

In this subsection theoretical LEED patterns will be discussed obtained from (2×4) or c(4×4) reconstructed GaAs(001) surfaces, including step and domain formation on the surface. In fig. 4.6 the expected LEED patterns from ideal (2×4) and c(4×4) reconstructed surfaces are given [PAS88]. When domains are formed, some spots may disappear due to destructive

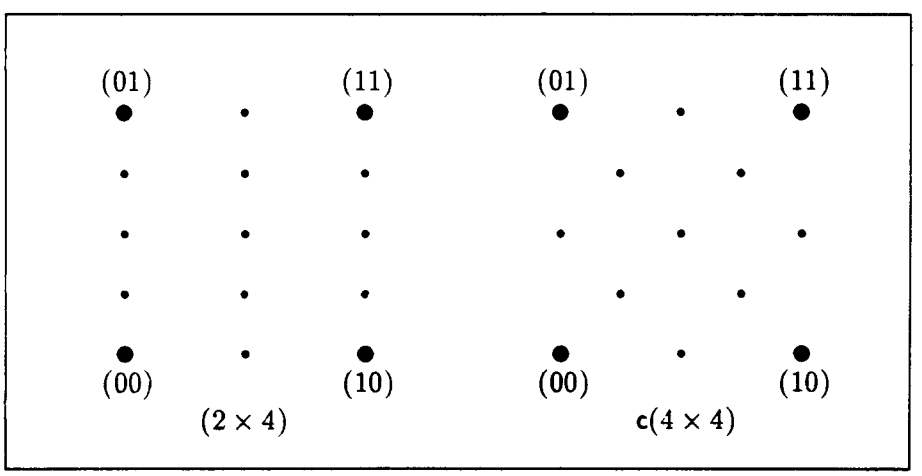

Figure 4.6: *LEED patterns for two reconstructions of GaAs(001)*

interference. For instance, fig. 4.7 shows two examples of translated (2×4) domains with the expected LEED pattern. In fig. 4.7.a (2×4) domains are arranged to produce the c(2×8) reconstruction. From the observed LEED pattern it might be incorrectly concluded that the surface has an (1×4) reconstruction. In fact, only few LEED observations are made which provides clear evidence for a c(2×8) structure [LAR88].

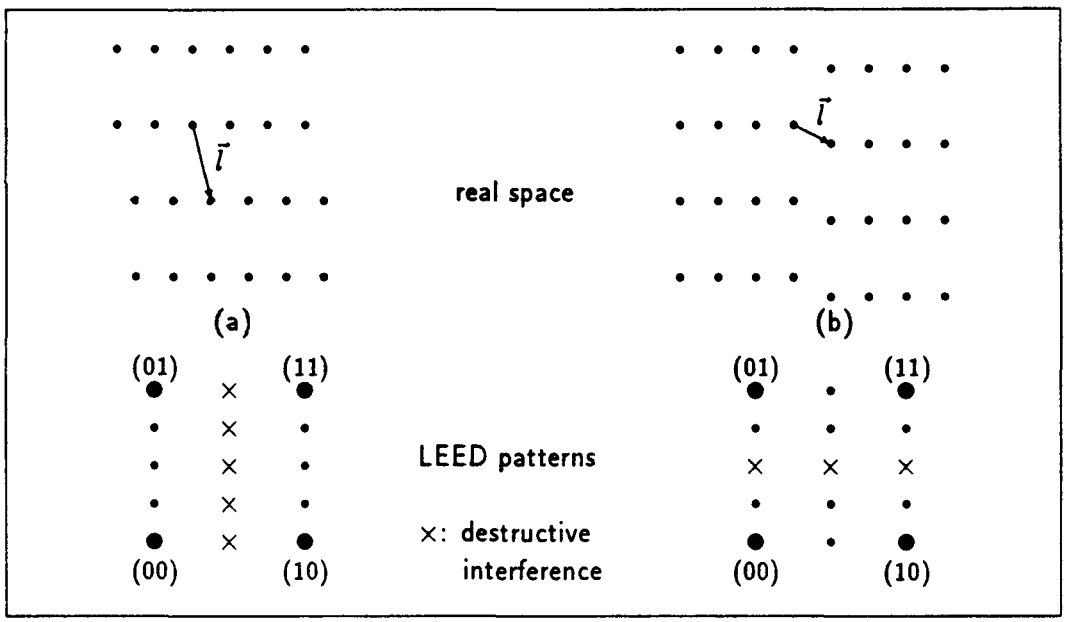

Figure 4.7: *Influence of domain formation on LEED patterns*

So far only spot positions have been described. With the formation of steps, the energy dependence of the spot intensities and spot shapes must be taken into account. A distinction can be made between step heights of either odd atomic or even atomic step height (fig. 4.8). The former separate terraces belonging to the two different sublattices, which are therefore

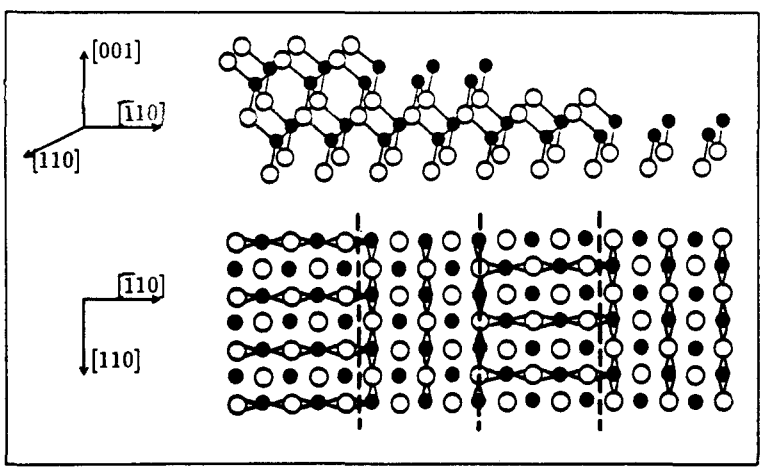

Figure 4.8: *Different steps on GaAs(001)*

called non-equivalent (i.e. a non-primitive step array). For inequivalent terraces the relative structure factors are considered to differ. The diffraction from stepped surfaces with non-equivalent terraces can be described by a quasi-kinematic approximation by assuming different structure factors for each kind of terrace and using the kinematic formalism otherwise [MOR87] (see subsection 2.2.5). Even atomic steps give rise to terraces belonging to the same FCC sublattice and so these terraces are equivalent and therefore the step array is

called primitive. For the different types of steps the lateral displacements $\vec{d}_{||}$ are:

$\vec{d}_{||} = \frac{1}{2}\vec{a}$ or $\vec{d}_{||} = \frac{1}{2}\vec{b}$ at a monoatomic step,

$\vec{d}_{||} = \frac{1}{2}\vec{a} + \frac{1}{2}\vec{b}$ at a diatomic step,

$\vec{d}_{||} = \frac{1}{2}\vec{a}$ or $\vec{d}_{||} = \frac{1}{2}\vec{b}$ at a three atomic step and

$\vec{d}_{||} = \vec{0}$ at a four atomic step.

For higher steps these displacements are repeated in the same sequence.

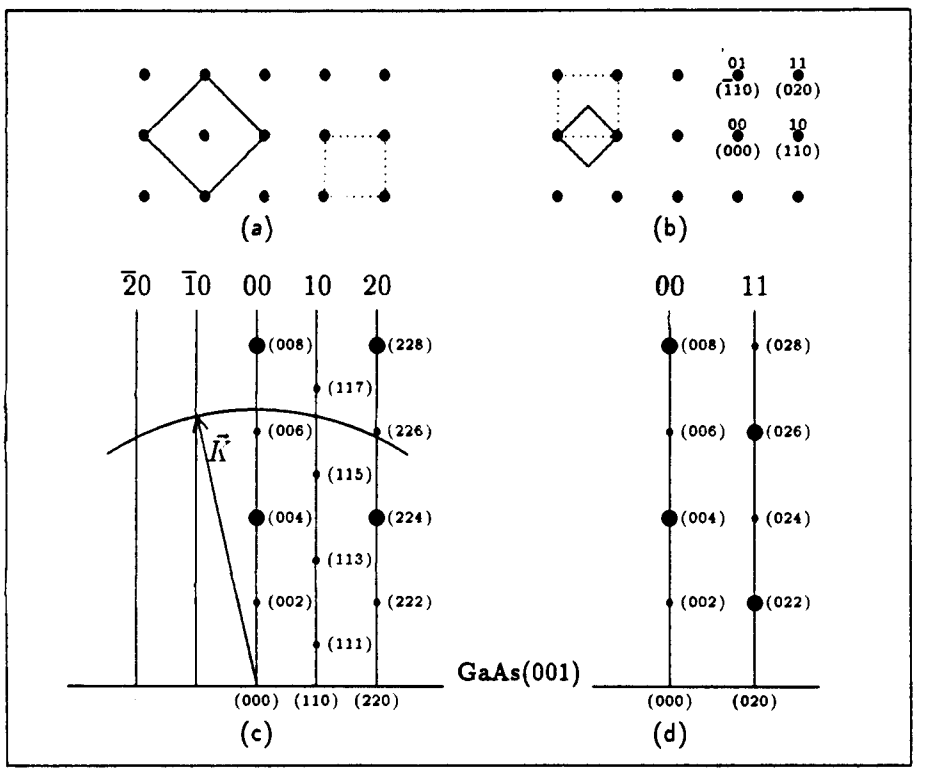

Figure 4.9: *Schematic view of the GaAs(001) surface in real (a) and in reciprocal (b) space; solid square: FCC cubic lattice cell, dashed square: unit cell. (c,d) Modified Ewald construction for SPA-LEED (E = 50 eV) demonstrating the two-dimensional lattice rods and the three-dimensional lattice points. Positions which yield sharp reflections in case of a monoatomic step array are marked with a bolder spot.*

In fig. 4.9.c,d the reciprocal lattice rods and three-dimensional lattice points are shown for the GaAs(001) surface. Only indices with *khl* = even or *hkl* = odd are allowed, due to the extinction law of FCC Bravais lattices. Every reciprocal lattice point on the rods satisfies eq. 2.36 ($\vec{K} \cdot 2\vec{d} = 2\pi S$) under condition that the surface contains diatomic steps. In that case the terraces are equivalent and sharp spots will occur at characteristic energies. The reciprocal lattice points which also satisfy eq. 2.36 for monoatomic steps are marked with a larger diameter. Terraces separated by monoatomic steps are non-equivalent. Therefore the spots will not be completely sharp, due to the different scattering factors. Furthermore no direction on the GaAs(001) can be found in which the terraces are equivalent, since the terraces contain

either As atoms or Ga atoms and thus have different scattering factors. This in contradiction with the Si(001) surface, where terraces separated by monoatomic steps are equivalent in the [100] direction [MOR87]. It can be seen in fig. 4.9.c that the (10) reflection is not affected by monoatomic steps. The fact that some reflections are not sensitive to non-primitive step arrays (i.e. monoatomic) gives reason to check several reflections at characteristic voltages for sharpness, in order to give a unique distinction between primitive and non-primitive step arrays.

Furthermore, it has been demonstrated that surface-sensitive electron diffraction measurements of steps on singular, but rough Si(001) surfaces are subject to a multiple scattering effect that can be misinterpreted as double atomic step heights [MAR87]. This phenomenon can occur in any surface in which adjacent terraces have different terrace structure factors (e.g. GaAs(001)). For example in fig. 4.10 a monoatomic step array is shown. The adjacent terraces are inequivalent and therefore have different scattering factors. The translation unit

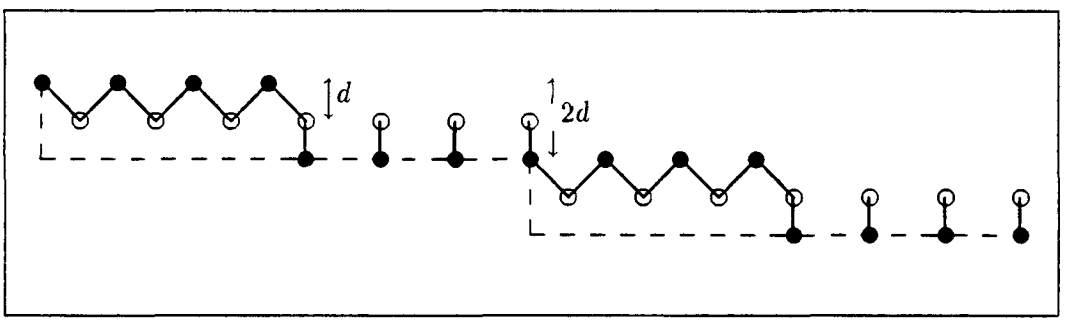

Figure 4.10: *Monoatomic step array showing diatomic periodicity*

then consists of two inequivalent terraces and a step. Normal to the surface the periodicity becomes $2d$ (diatomic) in stead of d (monoatomic).

Taking all topological features in account the LEED pattern may be very complicated.

4.1.3 Growth procedure of GaAs(001)

The sample were grown by Molecular Beam Epitaxy (MBE). In MBE a molecular beam containing a mixture of Ga and As_4 molecules is directed to the sample surface, yielding epitaxial growth when the sample is held at a proper temperature. The substrate was an GaAs(001) wafer, which was cleaned by an etching and annealing procedure. Observing the surface with RHEED after the cleaning process showed the As-stable (2×4) reconstruction. At a substrate temperature of 890 K GaAs was deposited at a growing rate of one monolayer per second, until 1 μm was grown. At the temperature of 890 K and under As-flux the (2×4) reconstruction was observed again. By cooling the sample under As-flux, the c(4×4) reconstruction was observed with RHEED. Because the sample had to be transported through air an amorphous As-cap of about 5 μm was deposited on the sample surface in order to reduce the oxidation. After preparation the sample surface reflected the light diffuse. For investigation of the GaAs(001)-(2×4) surface with SPA-LEED the As-cap has to be removed by heating the sample.

4.2 Experiments on GaAs(001)

4.2.1 Temperature measurements

The sample is heated by a Riber oven, which heats the sample from the back. The sample is mounted on a 1 mm thick Cu plate. In order to get a good heat contact between sample and Cu plate, the sample was sticked with Leitsilber on the plate. To measure the sample temperature a thermo-couple was mounted at the housing of the Riber oven. However, the discrepancy between the measured and real sample temperature appeared to be in the range 15-25% [GUN89]. Another instrument for temperature measurements is the infrared thermometer (Minolta/Land Cyclops 41). This thermometer measures the radiation emitted by the observed object in the wavelength region 1.1-1.7 μm. The measuring range of the thermometer is 523-1073 K. Because GaAs is transparant for this thermometer, the emissivity was installed at the emissivity of the non-oxidized copper plate, on which the sample was mounted. In this way the accuracy of the temperature reading is estimated to be 50 K. At this moment a new thermo-couple mechanism is under construction, which makes it possible to come in direct contact with the sample surface by means of a lever as soon as the sample holder is installed at the housing of the oven. The mechanism has already been tested and will be installed in the SPA-LEED vessel in early future.

4.2.2 Removal of the As-cap

In order to remove the As-cap and to restore the surface order and the stoichiometry after the removal of the As-cap, the sample is heated. The heating temperature is kept below the congruent evaporation temperature T_c. Below this temperature, decomposition is controlled by Ga evaporation and above this temperature it is controlled by As evaporation. For the GaAs(001) surface the congruent evaporation temperature T_c values 933 K [RAN81]. Since it is sufficient to take an heating temperature 100-150 K below T_c, the heating temperature was taken in the range 570-770 K. Several attempts have been made to remove the As-cap. Fig. 4.11 shows photographs made by Scanning Electron Microscopy of the GaAs(001) surface after different heating procedures. The scale of a photograph is given by the width of the black part in the beam at the bottom of the photograph.

At the photograph in fig. 4.11.a the edge of a sample with an unaffected amorphous As-cap is shown. In the substrate some fraction lines are observed due to the cleaving process. The As-cap is about 5 μm thick and is very rough. Therefore, no diffraction spots are observed with LEED.

During the heating of the samples the pressure in the SPA-LEED vessel increased due to the evaporation of the As-cap. Sample 1 was heated at 620-720 K, until the pressure in the vessel did not increase on further heating. Investigating the surface with LEED diffraction spots were observed belonging to the GaAs(001) bulk structure. Observing the sample with a light spot, still some diffuse reflecting streaks appeared. This was indicative for the fact that the As-cap might not have been entirely removed. This suggestion has been confirmed by SEM. In fig. 4.11.b can be seen that still rests of the As-cap are existing on the surface. The sample has also been studied with XPS and it was found that indeed the overlayers contained more As than the background.

The second sample was heated specifically longer (several hours) at the same temperature. This time the whole surface reflected the light brightly after the heating process and so the

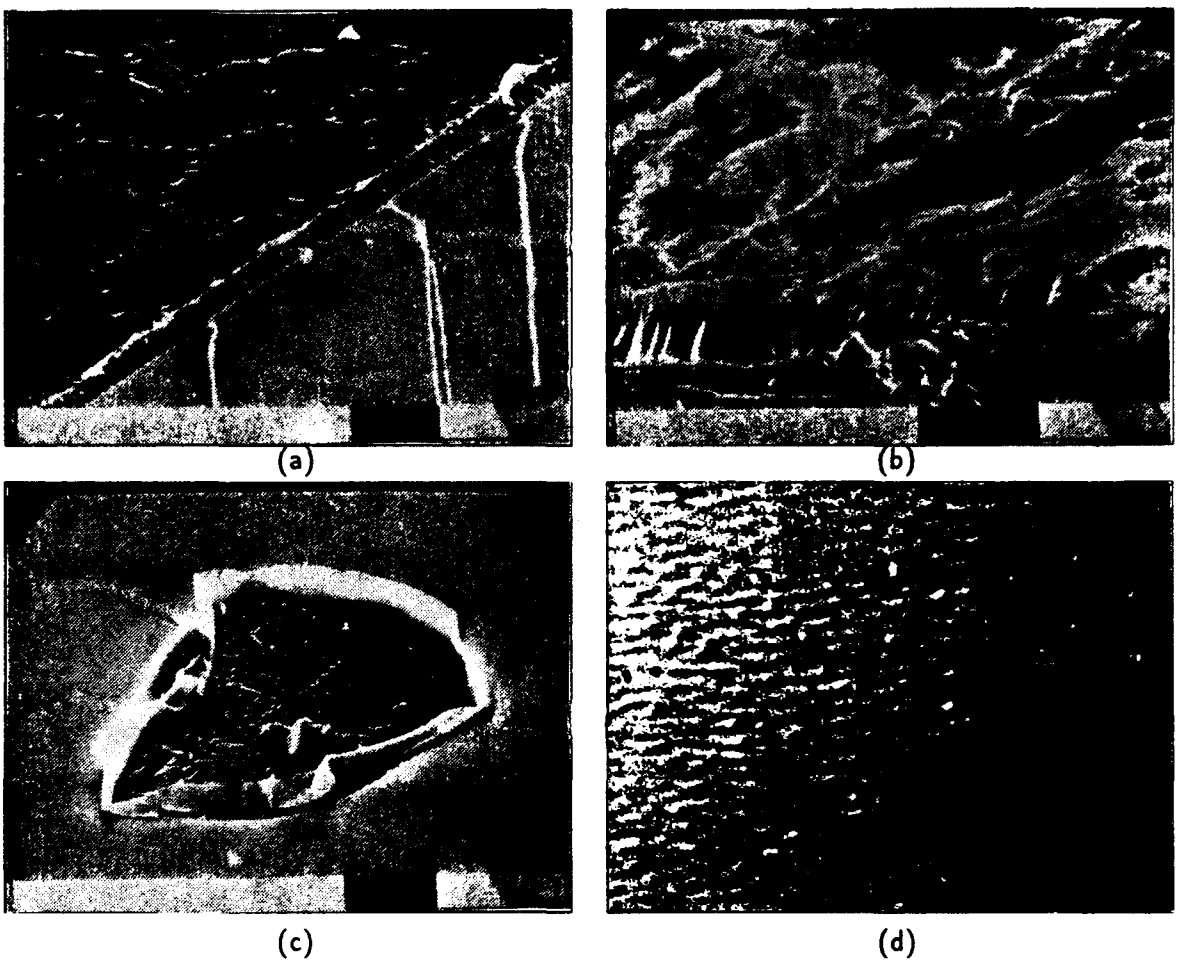

Figure 4.11: *The GaAs(001) surface after different heating procedures*

surface was considered clean. Again the observed diffraction pattern was consistent with the (1×1) structure of GaAs(001). Only for energies above $E = 100$ eV clear spots have been observed. After the surface was investigated with LEED, the sample was mounted in the SEM-apparatus. The surface was clean as expected, besides a few spots as shown in fig. 4.11.c.

The surface presented in fig. 4.11.d has been heated at 1070 K. At temperatures above T_c (933 K), As evaporates faster than Ga. The excess Ga is expected to coagulate into droplets, which are observed by SEM. The photograph made by SEM was not clear enough to print here. Fig. 4.11.d shows a photograph of the sample surface made by an optical microscope.

The experience in cleaning the GaAs(001) sample has learned that the complete removal of the As-cap is accompanied by the following conditions. The pressure in the SPA-LEED vessel decreases on further heating, the sample has a shiny appearance and of course diffraction spots are observed. Sample 5 was annealed at 670 K, until all three conditions were satisfied.

4.2.3 Experiments on GaAs(001)

Both sample 2 and 5 have been investigated for reconstructions and step heights at room temperature with SPA-LEED. No reconstructions have been found. The diffraction spots all belonged to the GaAs(001)-(1×1) structure. In fig. 4.12 two line scans are presented. If the (2×4) reconstruction would have been present at the surface, fig. 4.12.a should have shown one extra peak at half distance between the (00) and $(\bar{1}0)$ spot or three extra peaks at an integer times a quarter of the distance between the two main peaks. Fig. 4.12.b should have shown three extra peaks at an integer times a quarter of the distance between the (00) and (11) beam if the c(4×4) reconstruction would have been present at the GaAs(001) surface. Furthermore, an area scan containing the (00), (10), (01) and (11) spots also did not show extra spots (fig. 4.13).

The sample has also been investigated with RHEED [LEY89]. In this experiment the amorphous As-cap was removed by heating the sample at 670 K for a few minutes and subsequently at 570 K. During the heating the sample was observed by RHEED and after a few minutes the c(4×4) reconstruction was observed, which turned into the (2×4) reconstruction on further heating. When the sample was cooled down to room temperature the reconstruction vanished. Unfortunately, it was not possible to heat the sample and to make a study with LEED simultaneously, since the intensity decreased rapidly with higher temperatures.

In order to investigate the existence of steps on the GaAs(001) surface, the full width at half maximum (FWHM) of intensity profiles has been measured as a function of the electron energy for both the (00) and (11) spot.

In fig. 4.14 three intensity profiles of the (00) beam along the [110] direction, taken at different scatter conditions, are shown. The spot intensities are measured in the energy region 100-300 eV. Below 100 eV no diffraction spots are observed at room temperature. However, for energies below 100 eV very weak diffraction spots have been observed immediately after a heating treatment. The profile in fig. 4.14.a is taken at $E = 118$ eV, which is an in-phase condition for diatomic steps, but an out-phase condition for monoatomic steps. In fig. 4.14.c ($E = 170$ eV) for both step arrays the in-phase condition is valid. The intermediate energy ($E = 143$ eV) corresponds to an out-phase condition for diatomic steps and the intermediate condition $K_\perp d = \frac{1}{2}\pi$ for monoatomic steps. The peak-background intensity ratio is about a factor 10 worse compared to measurements presented in [WOL89]. The peak width of fig. 4.14.a is slightly larger than the peak width of fig. 4.14.c. In fig. 4.15 a comparison can be made between the spot profile of the direct reflection at $E = 170$ eV and 232 eV (same phase conditions as 118 eV). In this case the peak width at the out-phase condition for monoatomic steps (fig. 4.15.b) is smaller than the peak width at the in-phase condition. For the out-phase condition ($E = 143$ eV) the direct reflection clearly shows a diffuse background in the shape of a Lorentzian. The peak width for $E = 170$ eV is considerably smaller than the peak width for $E = 143$ eV.

This effect can also be noticed in fig. 4.12. Furthermore, in fig. 4.12.a the width of the $(\bar{1}0)$ reflection is smaller than the specular peak width. This is consistent with the fact that $E = 139$ eV approximates a characteristic energy in case of diatomic step heights for the $(\bar{1}0)$ reflection (see also fig. 4.9.c). The energy $E = 170$ eV used in fig. 4.12.b is a condition for a sharp (00) reflection (due to in-phase scattering for both monoatomic and diatomic step arrays) and a broadened (11) reflection. From fig. 4.9.d can be seen that the peak width oscillations for the (00) and (11) reflection have a phase shift of $K_\perp d = \pi$. Therefore the energy $E = 170$ eV is approximately an in-phase scattering condition for diatomic steps and

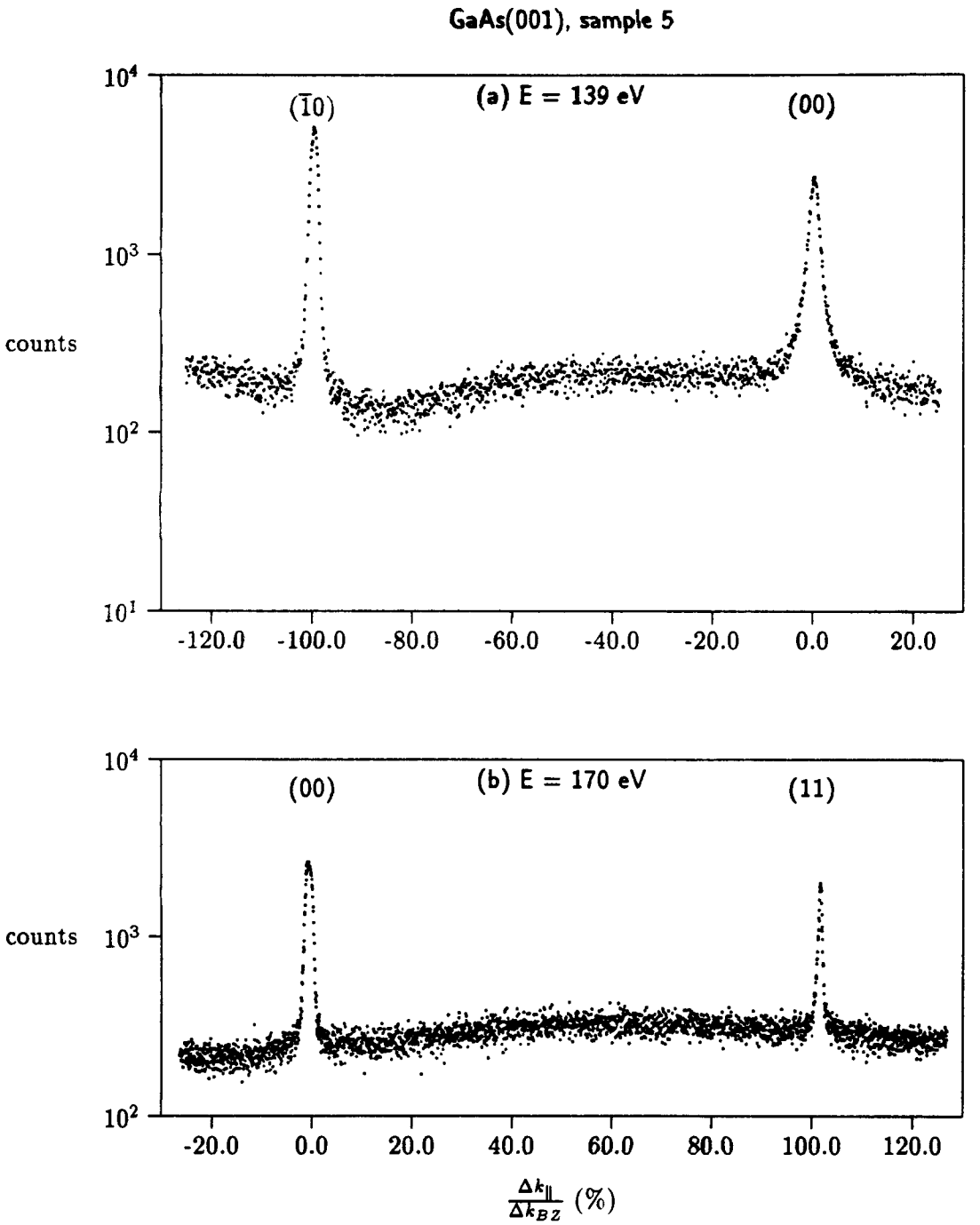

Figure 4.12: *Line scans of GaAs(001) from direct to a first order reflection*

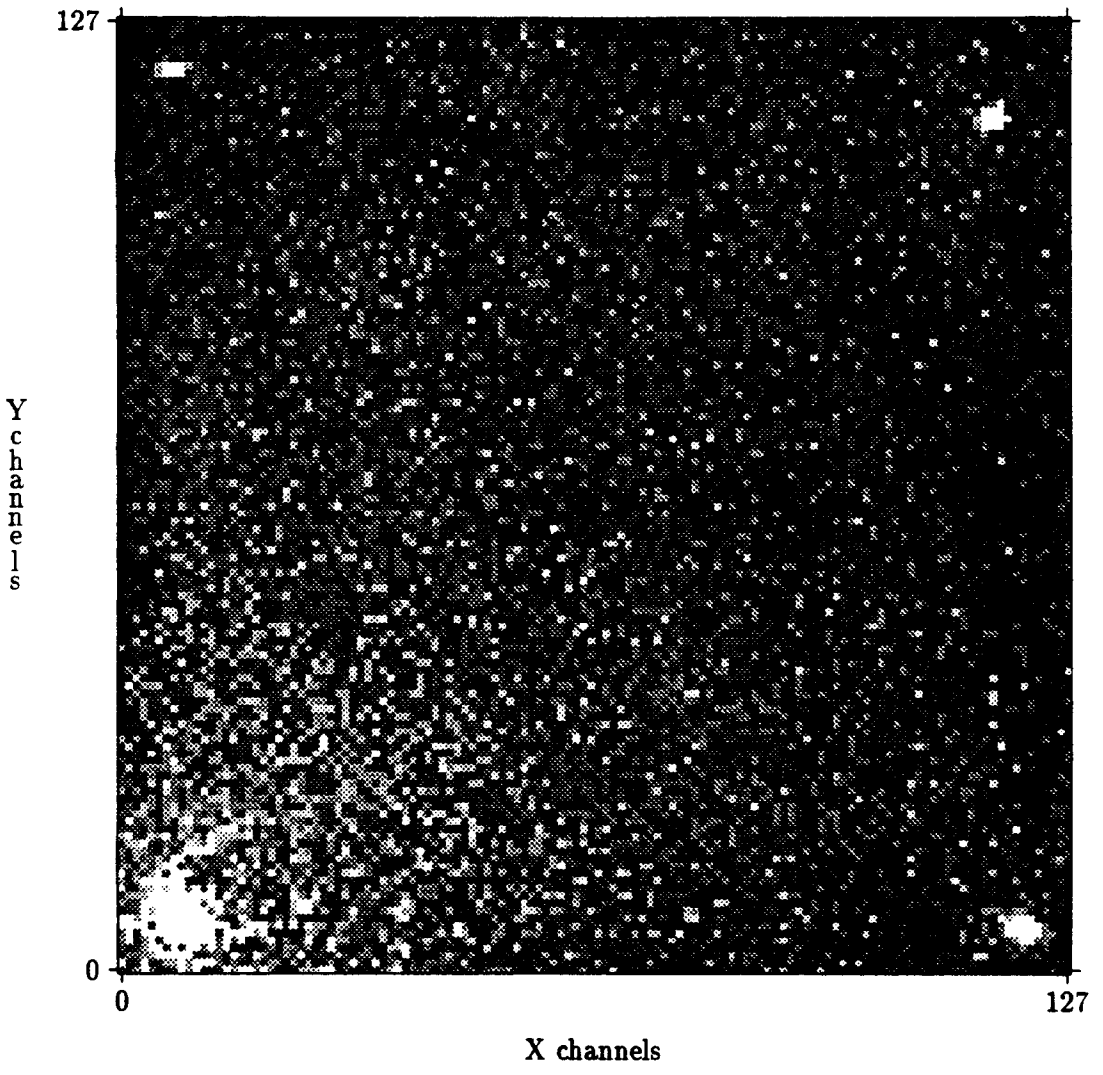

Figure 4.13: *Area scan showing zero and first order reflections*

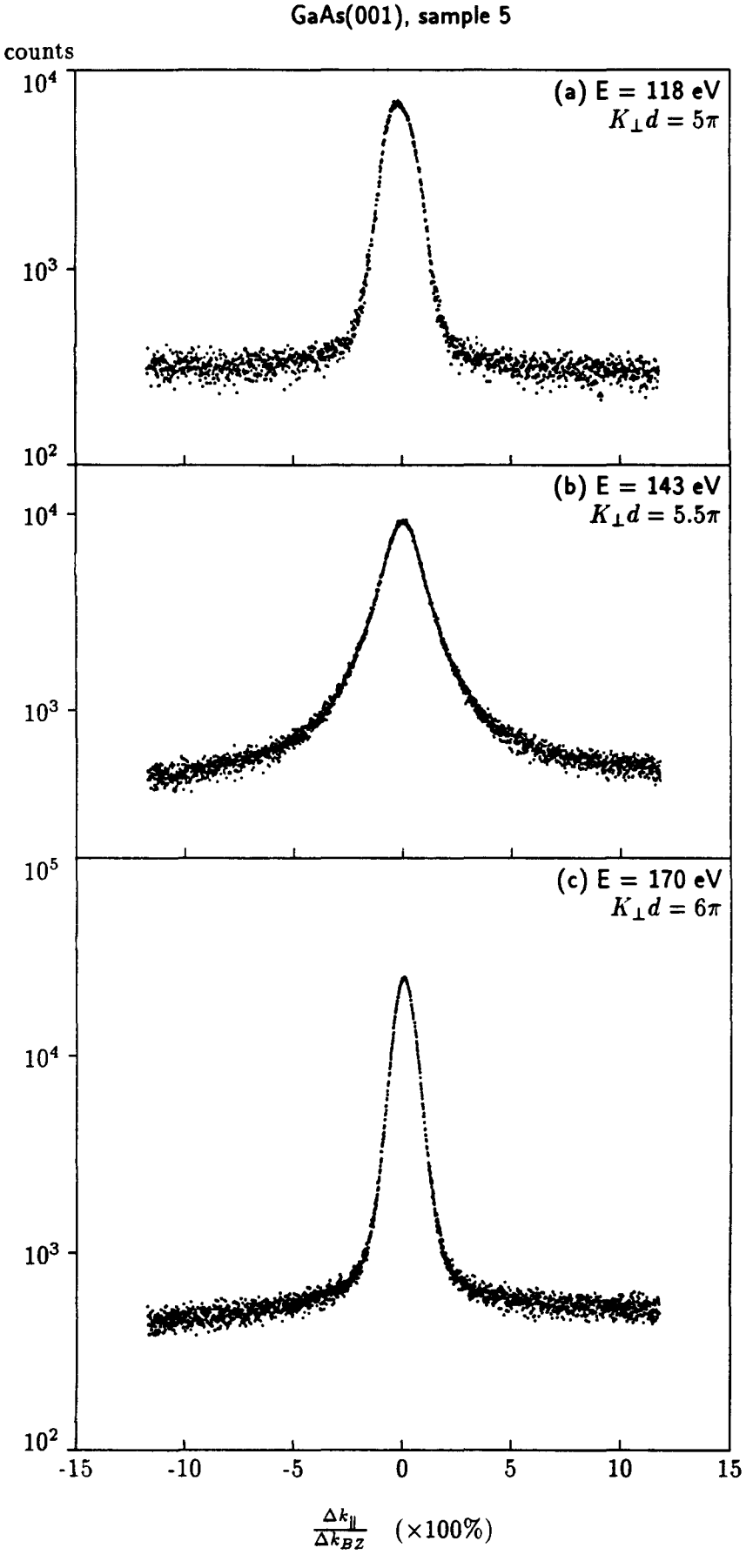

Figure 4.14: *Profile scans of the specular reflection of GaAs(001) for different energies*

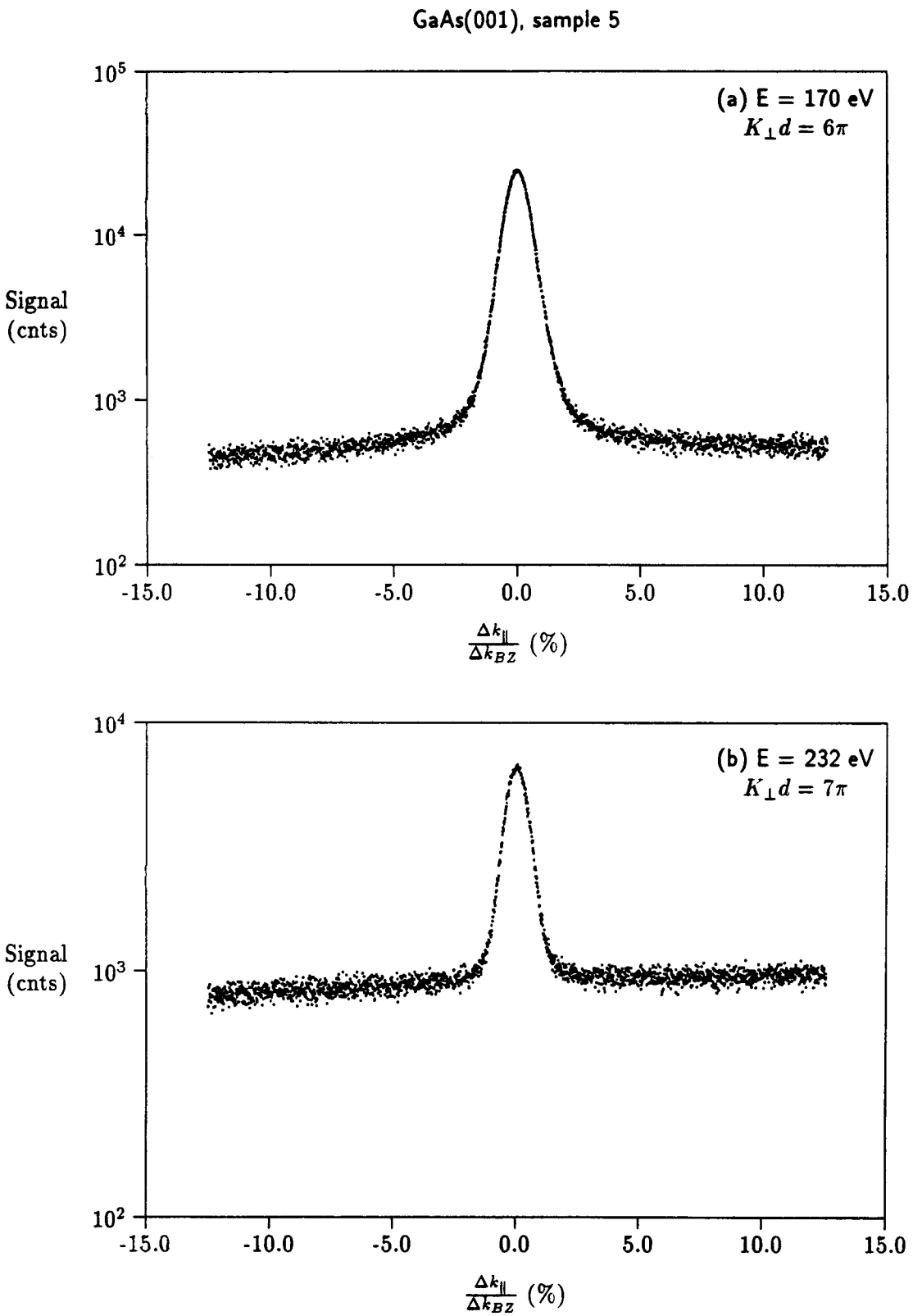

Figure 4.15: *Comparison of profile scans for two different scattering conditions*

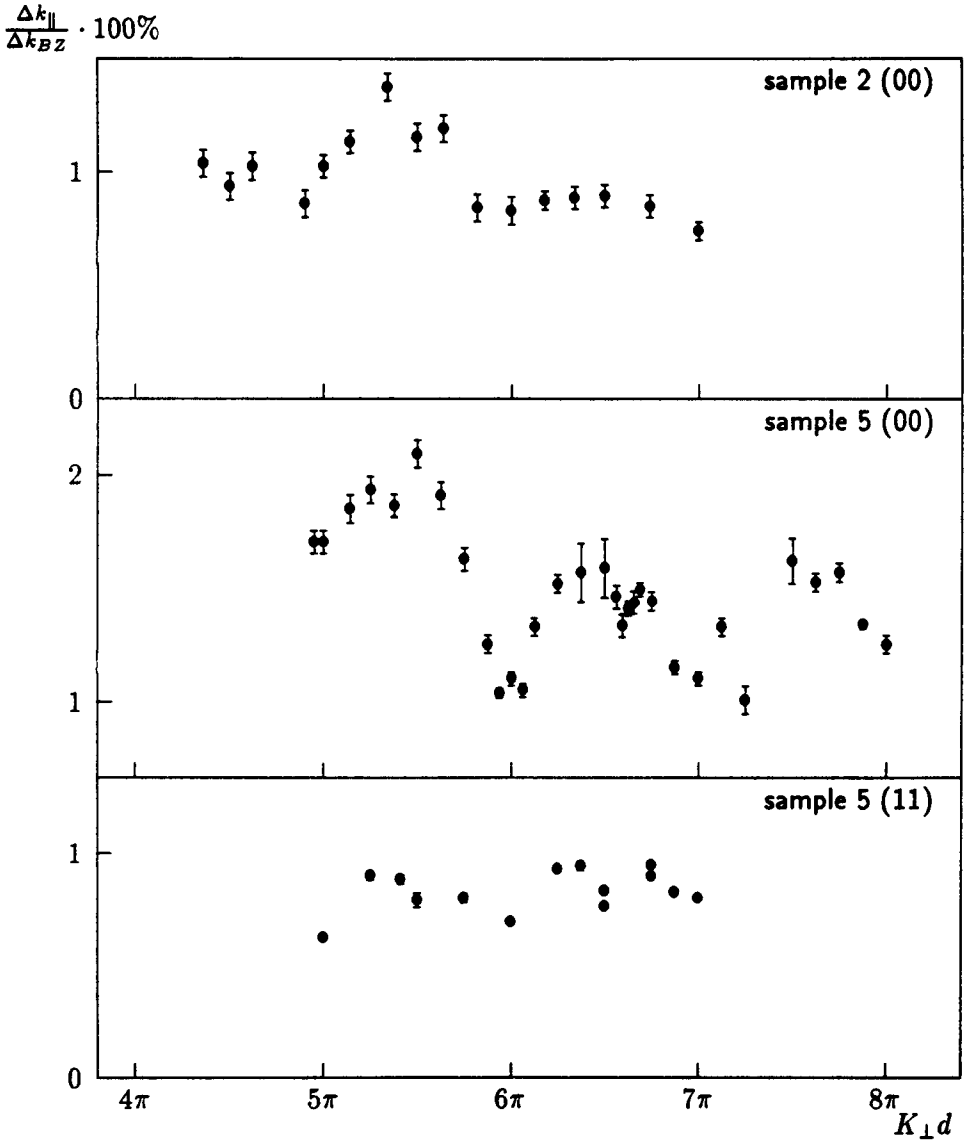

Figure 4.16: *FWHM of the (00) and (11) spot versus energy for sample 2 and 5*

an out-phase scattering condition for monoatomic steps, when the (11) reflection is observed. As can be observed in fig. 4.12.b the peak width of the (11) reflection is even smaller than the peak width of the direct reflection.

The results of the FWHM of the angular intensity profiles versus the energy for sample 2 and 5 are presented in fig. 4.16. The FWHM of the (00) and (11) spot varies characteristically with $K_\perp$ and contains information about the phase correlation from the different terraces involved. The amplitude of the oscillations is rather small (0.3-0.6%) compared to the amplitude of 2% in [WEI89]. The amplitude of the oscillations of the peak widths with energy is an indication for the amount of steps at the surface.

The GaAs(001) surface of sample 5 was also studied with LEIS. The surface revealed to have an excess As. During sputtering with Ne the As coverage decreased and the Ga coverage increased, but the former situation could be restored be annealing the surface.

4.3 Interpretation of the measurements

Only for energies above 100 eV a diffraction pattern has been observed. This pattern corresponds to the GaAs(001)-(1×1) structure. These observations lead to the conclusion that the toplayer is rather disordered. This disorder can be induced by the presence of carbon and carbon containing components on the surface [KER89,BRO89]. These kind of surface pollution may be caused by adsorption in the MBE-system. For energies below 100 eV the mean free path of electrons in a solid is below 0.5 nm (see fig. 2.2). The penetration depth of the electrons is therefore corresponding to the thickness of one atomic double layer of GaAs(001). For energies above 100 eV the interactions of the electrons are increasingly influenced by the scattering potential with the bulk periodicity and so the observed diffraction spots belong to the GaAs(001)-(1×1) structure. The considerable background in the spot profiles confirms the rather disordered state of the GaAs(001) surface at room temperature.

The period of the peak width oscillations might suggest that diatomic (and other even numbered) steps exist on the GaAs surface. The amplitude of the peak width oscillation is rather small, which indicates that the surface is fairly smooth.

With respect to the existence of steps on the surface, three situations have to be considered; the occurrence of solely monoatomic steps, solely diatomic steps and the occurrence of a combination of monoatomic and diatomic steps. In the first situation the surface consists of non-equivalent terraces. This means that for any diffraction condition a diffuse intensity arises, due to the fluctuation of the scattering amplitude along the surface (eq. 2.41). At the out-of-phase condition for monoatomic steps (118 eV and 232 eV) this broadening should reveal its maximum. However, neither in fig. 4.14.a nor in fig. 4.15.b a diffuse shoulder is noticeable.

Secondly, in the situation of only diatomic steps on the surface, the spot profiles are sharp at the in-phase condition (118 eV, 170 eV and 232 eV) and broadened at the out-of-phase condition (143 eV). This broadening clearly occurs in fig. 4.14.b. The peak widths at the in-phase condition have the tendency to become smaller with increasing energy. With increasing energy the electrons incident on the surface are more and more influenced by the scattering potential arising from deeper atomic layers (see fig. 2.2). Therefore the long range order might be better probed and sharper peaks occur at higher energies.

The third situation is the combination of monoatomic and diatomic steps. For this situation the spot profile for the out-of-phase condition for double steps (E = 143 eV) should

be composed of two Lorentzian profiles with different width. The probability for the occurrence of both steps can be determined if both components can be separated in fig. 4.14.b. This fitting procedure has not yet been performed. However, it is doubtful whether a fitting procedure at $E = 143$ eV will reveal reliable results, since in every spot profile the diffraction features corresponding to double step heights are dominant.

When the SPA-LEED system operates under optimum conditions a transfer width of about 100 nm is obtained. In this experiment the SPA-LEED system is aligned at 170 eV at settings corresponding with the manual. The best obtained transfer width in this way values 35 nm. In order to obtain the maximum transfer width experiments should be done on a specially prepared smooth sample with equivalent terraces (e.g. GaAs(110)).

LEIS experiments revealed that the toplayer of GaAs(001) has an excess of As atoms. Since the sticking probability for As on Ga is almost one and the sample contained an As-cap, it may concluded that if Ga terminated terraces were present at the surface, they may be covered with As. This is consistent with the dominance of double step heights observed in SPA-LEED measurements.

Summarizing, the investigated GaAs(001) surface is rather flat, with a limited number of mostly even-numbered steps and shows only short range order at room temperature.

Chapter 5

Conclusions and Recommendations

5.1 Conclusions

The SPA-LEED system equipped with the accurate and stable sample manipulator is very well suited to determine the angular intensity distribution within a large number of reflections.

From the existence of several intensity maxima in the direct reflection of highly oriented pyrolytic graphite, it is concluded that HOPG has a mosaic structure.

The first and higher order reflections are distributed over rings due to a random orientation of the crystallites. The observed maxima in the ring are not caused by dynamical scattering effects, but are a result of preferential orientations of the crystallites.

Scanning Tunneling Microscopy (STM) is very well suited to study the surface of HOPG on an atomic scale. SPA-LEED is very powerful in determining the distribution of the surface orientation of the crystallites. The combination of the results obtained with both techniques gives a complete picture of the surface topography of HOPG.

The considerable background and the fact that only the (1×1) diffraction pattern is observed above 100 eV on GaAs(001) at room temperature, leads to the conclusion that the surface has no long range order.

The oscillations of the peak width as a function of energy have a small amplitude and a period consistent with even-numbered atomic step heights (i.e. primitive step arrays). The small amplitude of the oscillation is an indication for a limited number of steps on the GaAs(001) surface.

Spot profile analyses lead to the conclusion that steps on the GaAs(001) surface are of double atomic step height. The existence of atomic steps can almost be excluded. This conclusion is supported by LEIS experiments, showing an excess of As in the toplayer of GaAs(001).

From the fact that the (2×4) reconstruction has been observed using RHEED at 420 K, it is concluded that at temperatures above room temperature long range order may exist on the surface.

5.2 Recommendations

In order to confirm the suggestion that the maxima in the first order ring of HOPG originate from preferential orientations of the crystallites, the entire ring should be measured. Preferential orientations of the crystallites will reveal the maxima to occur at every other 60°. As soon as sample rotation around the normal of the sample is possible, the entire ring can be measured.

To exclude broadening of the peaks due to the instrumental transfer width, the transfer width should be measured and corrected for. This measurement could be best performed on a specially prepared smooth sample with equivalent terraces only (e.g. GaAs(110)).

The RHEED experiment should be repeated with accurate temperature measurement of the observation of the reconstruction and the reversibility of the process should be checked.

Profile scans should be scaled logarithmic in counts. In this way the diffuse broadening is easier obtained in a visual inspection of a profile scan. The profile scans of the specular reflection should be fitted with Lorentzian for diffuse intensities and a Gaussian for sharp reflections.

REFERENCES

[ALT88] R. Altsinger, H. Bush, M. Horn and M. Henzler, Surf. Sc. **200** (1988), 235

[ASH76] N.W. Ashcroft and N.O. Mermin,'Solid State Physics', ed. D. Garbose Crane, Saunders College, (1976)

[BAC81] R.Z. Bachrach, R.S. Bauer, P. Chiaradia and G.V. Hansson, J. Vac. Sci. Technol. **18** (1981), 797

[BRO89] H.H. Brongersma, private communication

[BUS86] H. Bush and M. Henzler, Surf. Sc. **167** (1986), 534

[CHA82] D.J. Chadi, C. Tanner and J. Ihm, Surf. Sc. **120** (1982), L425

[CLA84] L.J. Clarke, in: 'Surface Crystallography: an Introduction to Low-Energy Electron Diffraction', John Wiley & Sons, (1984)

[DAV27] C.P. Davisson and L.H. Germer, Phys. Rev. **30** (1927), 705

[DAW82] L. Däweritz, Surf. Sc. **118** (1982), 585

[DOB82] P.J. Dobson, J.H.Neave and B.A. Joyce, Surf. Sc. **119** (1982), L339

[ELT89] S.J.E.A. Eltink, 'The magnetic properties of the Diluted Magnetic Semiconductors (Pb)SnMnTe', internal report TUE (1989)

[ERT85] G. Ertl and J. Küppers, 'Low-Energy Electrons and Surface Chemistry', Verlag Chemie (1985), second edition

[GUN89] P.L.J. Gunter, internal report TUE 1989

[HEN70] M. Henzler, Surf. Sc. **22** (1970), 12

[HEN74] M. Henzler and J. Clabes, Proc. 2nd Int. Conf. on Solid Surfaces (1974), Jap. J. Appl. Phys. Suppl. 2 Pt2 (1974), 389

[HEN77] M. Henzler, in: 'Topics in Current Physics: Electron Spectroscopy for Surface Analysis', ed. H. Ibach, Springer-Verlag, (1977)

[HEN84] M. Henzler, in: 'Dynamical Phenomena at Surfaces, Interfaces and Superlattices', ed. F. Nizzoli et al., Springer-Verlag, (1984)

[HEN85] M. Henzler, Surf. Sc. **152/153** (1985), 963

[HOR88] M. Horn, U. Gotter and M. Henzler, J. Vac. Technol. B **6** (1988), 727

[HOV86] M.A. van Hove, W.H. Weinberg and C.-M. Chan, 'Low-Energy Electron Diffraction', ed. G. Ertl, Springer-Verlag, (1986)

[KER89] T.M. Kerr, C.E.C. Wood, S.M. Newstead and J.D. Wilcox, J. Appl. Phys. **65** (1989), 2673

[LAG82] M.G. Lagally, in: 'Chemistry and Physics of Solid Surfaces IV', ed. R. Vanselow and R. Howe, Springer-Verlag (1982)

[LAR81] P.K. Larsen, J.H. Neave and B.A. Joyce, J. Phys. C: Sol. St. Phys. **14** (1981), 167

[LAR83] P.K. Larsen, J.H. Neave, J.F. van der Veen, P.J. Dobson and B.A. Joyce, Phys. Rev. B **27** (1983), 4966

[LAR88] P.K. Larsen and D.J. Chadi, Phys. Rev. B **37** (1988), 8282

[LEN84] C.S. Lent and P.I. Cohen, Surf. Sc. **139** (1984), 121

[LU82] T.-M. Lu and M.G. Lagally, Surf. Sc. **120** (1982), 47

[MAR87] J.A. Martin, C.E. Aumann, D.E. Savage, M.C. Tringides, M.G. Lagally, W. Moritz and F. Kretschmar, J. Vac. Sci. Technol. **A5** (1987), 615

[MOR87] W. Moritz, in: Proceedings of the NATO Workshop on RHEED (Plenum Press) 1987

[PAS88] M.D. Pashley, K.W. Haberern, W. Friday, J.M. Woodall and P.D. Kirchner, Phys. Rev. Lett. **60** (1988), 2176

[RAN81] W. Ranke and K. Jacobi, Prog. in Surf. Sc. **10** (1981), 1

[ROO87] A.G. Roosenbrand, internal report TUE (1987)

[SAU89] M. Sauvage-Simkin, R. Pinchaux, J. Massies, P. Claverie, J. Bonnet and N. Jedredy, Surf. Sc. **211/212** (1989), 39

[SCH86] U. Scheithauer, G. Meyer and M. Henzler, Surf. Sc. **178** (1986), 441

[WEA87] Handbook of Chemistry and Physics, 1^{st} student edition, ed. R.C. Weast (CRC Press, Florida) 1987

[WEB73] M.B. Webb and M.G. Lagally, Sol. St. Phys. **28** (1973), 301

[WEI89] W. Weiss, D. Schmeisser and W. Göpel, Surf. Sc. **207** (1989), 410

[WOL89] J. Wollschläger, J. Falta and M. Henzler, to be published

DANKWOORD

Graag wil ik iedereen bedanken die mij tijdens mijn afstudeerperiode bijgestaan heeft. Allereerst wil ik prof.dr. H.H. Brongersma bedanken voor zijn interesse in mijn werk en Bert Roosenbrand voor zijn dagelijkse begeleiding en vele stimulerende bemoedigingen. Bij deze wil ik Bert dan ook voordragen als Begeleider Van Het Jaar. Verder gaat mijn dank uit naar Camiel Severijns (1^e keer).

De volgende personen wil ik met name bedanken: Eddy van Egmond (voor XPS-metingen), Stephan Eltink (je-weet-wel-waarvoor), Kees van Leerdam (voor LEIS-metingen), Harry Maaskamp (voor SEM-metingen), Maarten Leys en Willem van de Vleuten (voor de GaAs-preparaten en RHEED-metingen), Camiel Severijns (voor de computer hulp; 2^e keer) en Gerard Weyers (voor de technische ondersteuning).

Tenslotte wil ik alle medewerkers en studenten van de groep FOG (dus ook Camiel Severijns; 3^e keer) bedanken voor de prettige werksfeer.

Mariëlle v. Beckhoven

Eindhoven, 6-7-1989